1 **Title:**

2 **Tracking infectious entry routes of SARS-CoV-2**

3

4 **Authors:**

5 Alex J.B. Kreutzberger [a,b], Anwesha Sanyal [a,b], Anand Saminathan [a,b], Louis-Marie Bloyet

6 [c], Spencer Stumpf [c], Zhuoming Liu [c], Ravi Ojha [d], Markku T. Patjas [e], Ahmed Geneid [e],

7 Gustavo Scanavachi [a,b], Catherine A. Doyle [f], Elliott Somerville [b], Ricardo Bango Da

8 Cunha Correira [a,b], Giuseppe Di Caprio [b,g], Sanna Toppila-Salmi [h], Antti Mäkitie [e], Volker

9 Kiessling [i], Olli Vapalahti [d,j,k], , Sean P.J. Whelan [c,*], Giuseppe Balistreri [d,j,l *], and Tom

10 Kirchhausen [a,b,g,*]

11

12 **Affiliations:**

13 [a] Department of Cell Biology, Harvard Medical School, 200 Longwood Av, Boston, MA 02115,

14 USA

15 [b] Program in Cellular and Molecular Medicine, Boston Children's Hospital, 200 Longwood Av,

16 Boston, MA 02115, USA

17 [c] Department of Molecular Microbiology, Washington University in Saint Louis, 660

18 South Euclid Avenue, Saint Louis, MI 63110, USA

19 [d] Department of Virology, Faculty of Medicine, University of Helsinki, Helsinki, Finland

20 [e] Department of Otorhinolaryngology and Phoniatrics, Head and Neck Surgery, University of

21 Helsinki and Helsinki University Hospital, Helsinki, Finland.

22 [f] Department of Pharmacology, University of Virginia, Charlottesville, VA 22903

23 [g] Department of Pediatrics, Harvard Medical School, 200 Longwood Ave, Boston, MA 02115, USA

24 [h] Department of Allergy, University of Helsinki and Helsinki University Hospital, Helsinki, Finland.

25 [i] Center for Membrane and Cell Physiology and Department of Molecular Physiology and

26 Biological Physics, University of Virginia, Charlottesville, VA 22903

27 [j] Department of Veterinary Biosciences, University of Helsinki, Helsinki, Finland

28 [k] Virology and Immunology, Helsinki University Hospital Diagnostic Center (HUSLAB), Helsinki,

29 Finland

30 [l] The Queensland Brain Institute, University of Queensland, Brisbane, Australia

31

32 [*] Corresponding authors.

33 kirchhausen@crystal.harvard.edu (T.K.)

34   giuseppe.balistreri.fi (G.B.)

35   spjwhelan@wustl.edu (S.P.J.W.)

36

One sentence summary:

38   Detailed molecular snapshots of the productive infectious entry pathway of SARS-CoV-2 into cells

ABSTRACT:

SARS-CoV-2 cell entry starts with membrane attachment and ends with spike-protein (S) catalyzed membrane fusion depending on two cleavage steps, one usually by furin in producing cells and the second by TMPRSS2 on target cells. Endosomal cathepsins can carry out both. Using real-time 3D single virion tracking, we show fusion and genome penetration requires virion exposure to an acidic milieu of pH 6.2-6.8, even when furin and TMPRSS2 cleavages have occurred. We detect the sequential steps of S1-fragment dissociation, fusion, and content release from the cell surface in TMPRRS2 overexpressing cells only when exposed to acidic pH. We define a key role of an acidic environment for successful infection, found in endosomal compartments and at the surface of TMPRSS2 expressing cells in the acidic milieu of the nasal cavity.

Significance Statement:

Infection by SARS-CoV-2 depends upon the S large spike protein decorating the virions and is responsible for receptor engagement and subsequent fusion of viral and cellular membranes allowing release of virion contents into the cell. Using new single particle imaging tools, to visualize and track the successive steps from virion attachment to fusion, combined with chemical and genetic perturbations of the cells, we provide the first direct evidence for the cellular uptake routes of productive infection in multiple cell types and their dependence on proteolysis of S by cell surface or endosomal proteases. We show that fusion and content release always require the acidic environment from endosomes, preceded by liberation of the S1 fragment which depends on ACE2 receptor engagement.

Main Text:

SARS-CoV-2 cell entry begins with engagement at the cell-surface and ends with deposition of the viral contents into the cytosol by membrane fusion. The first step is binding of the viral spike protein (S) with its cellular receptor, angiotensin converting enzyme (ACE2) (*1–4*). The last step delivers the viral genomic RNA in association with the nucleocapsid protein (N), which is removed for translation of the input genome (*5, 6*). Proteolytic activation of S by additional host-cell factors is necessary for it to function as a fusogen. Cleavage of S by furin in producer cells (*7*) generates the S1 receptor binding subunit non-covalently associated with the S2 fusion subunit. The S protein is cleaved by cell surface or endosomal proteases during virion entry into host cells, that activate the viral fusion machinery (*1, 8–10*). This entry associated proteolysis of S has led to the current model of two routes of infectious cell entry: fusion of viral and cellular membranes at the host-cell surface or fusion following endosomal uptake (*6*).

The cellular proteases that are involved in processing S during entry include the transmembrane serine proteases TMPRSS2 or TMPRSS4 found at the cell surface (*1, 8*), and the endosomal cathepsins that require the acidic milieu of the compartments in which they are enriched (*1, 10*). Processing of S by TMPRSS proteases or by cathepsins, at a site designated S2', depends on prior cleavage at the furin site in the producer cells (*7, 11, 12*). TMPRSS cleavage has been thought to result in infection from the plasma membrane and cathepsin cleavage, in cells lacking TMPRSS activity, with infection from endosomes (*5, 6*). Chemical inhibitors of TMPRSS or cathepsin proteases in cells in culture indeed show that infection of some cell types is more sensitive to inhibition of endosomal cathepsins whereas others are more sensitive to inhibition of TMPRSS proteases (*1, 9*). TMPRSS inhibitors such as camostat and nafamostat are in clinical development as SARS-CoV-2 therapeutics, further highlighting the need to understand how entry pathways depend upon specific proteases.

To analyze the routes of cellular uptake that lead to successful fusion and release of virion contents into the cytoplasm, we developed a set of new tools that allow direct visual tracking of the uptake of single virions and release of their contents. Using a chimeric vesicular stomatitis virus (VSV) in which SARS-CoV-2 S has replaced the endogenous glycoprotein gene (G), we modified the virus to permit the separate tracking of the S protein and the viral contents. We engineered a structural component of the replicative core of VSV, the phosphoprotein (P), to append to its amino terminus enhanced green fluorescent protein (eGFP), for tracking the virion content. This eGFP-P chimeric virus is structurally fluorescent and depends upon S for entry. We

95   also sparsely labelled the S protein by direct conjugation with a fluorescent dye, allowing us to

96   visualize the steps of entry, from S1 fragment release to membrane fusion, including virion content

97   release into cells during productive infection. We have found that content release requires acidic

98   pH and that it occurs principally from endosomes irrespective of the cell type and irrespective of

99   the dependence of the virus on TMPRSS2 or cathepsin-mediated processing of S. Only mild

100 acidification of the medium allows efficient entry at the plasma membrane. We correlate our

101 findings with studies of infection by several human isolates of SARS-CoV-2.

102

103 **RESULTS**

104 **Cell entry of individual virions mediated by SARS-CoV-2 S**

105 We used live-cell fluorescence microscopy to monitor uptake of single VSV-SARS-CoV-2 virions

106 that depend upon SARS-CoV-2 S for infection (Wuhan Hu-1 isolate and Delta and Omicron

107 variants, chimeras generated as described: see Methods and (*13*)) and for the Wuhan variant

108 also containing a fluorescent internal structural protein, P, fused at its amino terminus to eGFP

109 (eGFP-P) (Fig. S1). We counted the number of tagged particles internalized 1 hr post inoculation

110 at MOI 0.5 and found 50-70 particles in Caco-2, Calu-3, and Vero cells, but about three times that

111 number in Vero-TMPRSS2 cells, which overexpress TMPRSS2 (Fig. S1D, E), presumably

112 because of more efficient TMPRSS2 cleavage in the high expression cell line. Examination of the

113 labeled virions by spinning-disc confocal microscopy showed distinct, diffraction-limited puncta

114 with a single, Gaussian distribution of fluorescent intensities (Fig. S2A), consistent with the

115 presence of single virus particles and absence of virion aggregates. We also labeled the S protein

116 sparsely with the fluorescent dye Atto565 NHS ester (25-35 dyes per virion), with minimal effect

117 on particle infectivity (Fig. S2A-D). The double labeling allowed us to track the viral S protein

118 separately from the virion contents.

119

120 **SARS-CoV-2 S-mediated entry requires endocytic uptake**

121 We used live-cell volumetric, lattice-light-sheet fluorescence microscopy (LLSM) (*14*) to obtain 3D

122 views of virion cell-entry over time during their uptake into cells (Figs. 1A-E, Fig S3). We incubated

123 cells for 8 min, transferred them to the LLSM, and recorded sequential 3-D stacks from a single

124 cell, acquiring a full stack every 2 sec, for 10 min (300 stacks total). We then moved quickly to

125 an adjacent cell and recorded a similar 10 min series of 300 stacks, after which we moved finally

126 to a third neighboring cell, for 10 min. The sequence of representative 10-plane projections in

127 Fig. 1B shows that particles attached to the cell surface during the initial 8 min incubation, followed

128 by efficient internalization at later time points. The figure shows images from Vero-TMPRSS2

129   cells; we obtained similar results for Vero, Caco-2 and Calu-3 cells, as shown in Fig S3. The views

130   from 20- and 30-minutes post-inoculation also showed many examples of intracellular spots

131   labeled with eGFP-P only, representing delivery of the VSV ribonucleoprotein core (RNP) into

132   cells visualized as the separation of fluorescent eGFP-P from the membrane-bound, Atto565

133   labelled S glycoprotein.

134

135   We confirmed that the views in Fig 1B reflected the outcome of sequential internalization and

136   RNP delivery events by tracking individual particles in the volumetric time series acquired using

137   LLSM (Fig. 1C). Single virions attached to cells during the 8 min period following addition of virus,

138   and ~ 90% (1508/1692) of the attached particles had internalized during the 30 min time course,

139   as recorded in 60 time-lapse 3D videos from 20 cells. The representative 10-plane projection in

140   Fig. 1C obtained during the initial 10-minute interval shows several single-particle examples of

141   virion internalization and three events of RNP core release (for similar results with Vero, Caco-2

142   and Calu-3 cells, see Fig S3). The highlighted example in Fig. 1C and the complete ortho

143   projection in Fig. 1D show a fluorescent spot corresponding to a virus particle, first captured at

144   the cell surface, then undergoing rapid directed movement towards the cell interior, due to

145   endocytosis and intracellular traffic of virus-containing vesicles. Dissociation of the eGFP-P from

146   the Atto565 signals marks delivery of the genome into the cytosol (see also Figs. S3-S7). In a

147   total of 60 Caco-2, Calu-3, Vero and Vero-TMPRSS2 cells, we detected separation of signals at

148   an intracellular location for 138/1692 trajectories during the 30-min interval starting two minutes

149   after an initial 8-minute inoculation (Fig. 1E), and only one dissociation event at the cell surface

150   (for a Vero-TMPRSS2 cell). The fluorescent signals from eGFP-P released in these times frames

151   remained stable and punctate in the cytosol during the duration of the 10 min acquisition, and any

152   released eGFP-P in the cytosol at the outset of the second or third 10 min time series remained

153   stable for the entire 10 min recording. Moreover, we never observed uncoated (delivered)

154   particles (i.e., released eGFP-P) in the early frames of the time lapse from the first cell. These

155   observations rule out the possibility of rapid, early entry events from the cell surface or from

156   endosomes during the "blind" 8 minutes during inoculation, and we conclude that an endocytic

157   route accounted for all but one of the detected VSV-SARS-CoV-2 fusion events in these

158   experiments.

159

160   Analysis of mean square displacement (MSD) curves from three-dimensional, single-particle

161   trajectories allowed us to determine the dynamic regime of the particle at any time point after

162   attachment. The alpha coefficient (α) in the anomalous diffusion equation ($<r^2> = 6Dt^{\alpha}$)

163   corresponds to confined motion (α < 0.8) for the virus attached to the cell surface, directed motion

164   (α >1.2) for intracellular particles with co-localized Atto565-labelled S and eGFP-P labelled RNP,

165   presumably associated with endosomes, and Brownian motion (0.8< α <1.2) for eGFP-P spots

166   diffusing in the cytosol. The results shown in Fig. 1F (which corresponds to the viral particle traced

167   in Figs. 1 C and D) and the summary for all tracked particles in Fig. 1G (see also Fig. S3-S7)

168   illustrate the moment at which an RNP escapes into the cytosol (α = 1.07), while the tagged S

169   remains associated with an endosome (α = 1.93, see below).

170

171   The chimeric VSV particles are roughly 80 by 200 nm (*15*, *16*) and appear in the microscope as

172   diffraction-limited spots. Endosomes typically range in diameter from 300-1000 nm (*17*). Thus, a

173   subset of fluorescent endosomes are larger than the diffraction limit, facilitating use of an

174   increased apparent size of an Atto565 fluorescent spot as a proxy for viral membrane fusion with

175   the surrounding (larger) endosomal membrane (Fig. S8). Using this approach, we detected fusion

176   in 17 $\pm$ 4 % (n = 20 virions), 28 $\pm$ 2% (n = 61 virions), 23 $\pm$ 2% (n = 27 virions), and 27 $\pm$ 6% (n =

177   30 virions) of the traces in Vero, Vero-TMPRSS2, Caco-2 or Calu-3 cells, respectively. All the

178   events coincided with release into the cytosol of the eGFP-P labeled RNP core of VSV (Figs. 1E,

179   S3, S7). We did not observe release of the virion contents at the plasma membrane (Figs. 1E,

180   S3-S7), indicating that S-mediated infection of cells only occurred through an endocytic pathway.

181

SARS-CoV-2 S-mediated infection requires endocytosis

183   Dynamin, a large GTPase required for cargo uptake in clathrin-mediated or fast endophilin-

184   mediated endocytosis (*18*), is susceptible to interference by a dominant negative mutant, K44A

185   (*19*). To test whether dynamin-dependent endocytosis is necessary for SARS-CoV-2 S mediated

186   infection, we transiently over expressed the dominant-negative mutant in Caco-2, Calu-3, Vero

187   and Vero-TMPRSS2 cells. We monitored the effect on infection of these cells by VSV-SARS-

188   CoV-2 that expresses eGFP as a marker of infection (VSV-eGFP-SARS-CoV-2) according to the

189   scheme summarized in Fig S9A, and we quantified infection by single-cell imaging at 8 hours post

190   inoculation. In control cells, to achieve comparable infectivity we used 10 times more VSV-SARS-

191   CoV-2 for Caco-2 and Calu-3 cells than for Vero or Vero-TMPRSS2 over-expressing TPMRSS2

192   (Figs. S9B, C). Irrespective of the cell type, infection was inhibited by the dominant negative

193   dynamin mutant (Fig 1H) or by addition of dynasore-OH, a small molecule dynamin inhibitor (*20*)

194   (Fig. 1I). Dynasore-OH addition at 1h post-inoculation had no effect on viral infectivity, consistent

195   with inhibition of an early, entry-related event, but not with later inhibition of viral gene expression

196   (Fig. S9C). We previously reported that S mediated infection of cells by VSV-SARS-CoV-2

197 correlates well with infection by SARS-CoV-2 (*9*, *13*, *21*, *22*). In accord with that correlation,

198 dynasore-OH also inhibited infection of Calu-3 and Vero-TMPRSS2 cells by a SARS-CoV-2

199 Wuhan (B.1) clinical isolate (Fig 1J). These results show a critical role for endocytosis in SARS-

200 CoV-2 infection of multiple cell types in culture including cells that express TMPRSS2.

201

202 **Viral entry from endosomes**

203 Our data show that internalized virus particles reached internal membrane compartment(s) from

204 which fusion and genome entry into the cytosol occurred. To establish the identity of the(se)

205 endosomal compartments, we used live-cell LLSM to track particles entering SVG-A cells

206 ectopically expressing ACE2, or both ACE2 and TMPRSS2, and gene-edited for fluorescent

207 labeling of specific endosomal compartments. (Fig. 2A, S10). Single particle tracking of 6815

208 viruses over a 50 min period starting from 30 minutes post inoculation of cells revealed VSV-

209 SARS-CoV-2 particles trafficked from the cell surface to early endosomes marked with early

210 endosomal antigen 1 fused to the fluorescent protein Scarlett (EEA1-mScarlett) and subsequently

211 to late endosomes/lysosomes marked with a Halo-tagged version of the cholesterol transporter

212 Niemann Pick C1 NPC1-Halo-JFX646 (examples for single virions shown in Fig 2 B, C, S11-S12).

213 We only detected particles located in the interior localizing with the endosomal markers in early

214 frames of the time lapse from the first cell taken at the end of the 30 min inoculation period. Like

215 with the other cells, these observations also rule out for SVG-A cells the possibility of entry events

216 from the cell surface or from endosomes during the 30-min inoculation period.

217

218 To establish the location of the compartments from which the virion contents were released, we

219 identified the point at which the trajectory of the eGFP-P signal changed from directed (α >1.2) to

220 Brownian (0.8< α <1.2) concomitant with a loss of co-localization with endosomal markers

221 (examples for single virions shown in Fig 2 D, E, S13-S14). All entry events occurred from

222 compartments marked with either EEA1 or NPC1 in cells expressing TMPRSS2, and only from

223 NPC1-compartments in cells lacking TMPRSS2 (Fig. 2 F, S15).

224

225 **Release of S1 at the surface of cells expressing TMPRSS2**

226 Membrane fusion mediated by S depends on its proteolytic cleavage and dissociation of the S1

227 fragment (*6*). Cleavage alone does not release S; the required trigger is ACE2 binding. Addition

228 of soluble ACE2 ectodomain to VSV-SARS-CoV-2 particles activated by trypsin, to bypass

229 TMPRSS2, released about 70% of the Atto 565 label, a reasonable estimate of the fraction of S1

230 rather than S2. In live-cell imaging experiments with TMPRSS2 expressing cells, we noted a

231   partial loss of Atto 565 intensity from labeled VSV-SARS-CoV-2 particles after they attached to
232   the cell surface (Fig. S19). In these experiments, we used a microfluidics device to introduce virus
233   to cells while in the LLSM, enabling us to detect attachment directly. We interpreted the loss of
234   Atto 565 signal as S1 dissociation, and we took it as a proxy for cleavage by TMPRSS2 at the S2'
235   site on an ACE2-attached spike protein. Dissociated S1 will remain attached to ACE2 for some
236   time, and in about ~2 % of the events, we could indeed detect lateral spreading (interpreted as
237   diffusion in the plasma membrane) associated with the abrupt partial reduction of the punctate
238   Atto 565 signal. We found ~25% loss of the Atto 565 signal per particle in ~ 78% of particles at
239   the surface of Vero-TMPRSS2 cells expressing TMPRSS2 (Fig. 3 A-D) within the first 10 min of
240   LLSM single-particle tracking (Fig. 1E). In all cases the loss was in a single step with a half time
241   of 2 sec or less (Fig. 3B and Fig. S16). The signal reduction, which preceded endocytosis, was
242   never associated with RNP delivery (e.g., eGFP-P) from the cell surface (Fig. 1E, cell #1), except
243   under the special circumstances of slightly acidic medium during inoculation as described in the
244   following section (Fig. 3 E-J and Fig. 4). The signal loss at the cell surface depended strictly on
245   TMPRSS2 activity, as it was inhibited by 10 μM Camostat and was absent in Vero cells lacking
246   TMPRSS2 (Fig 3D). The decrease in punctate intensity, which we interpret as release of S1,
247   occurred in less than 5% of particles attached to Caco-2 or Calu-3 cells, which naturally express
248   TMPRSS2 (Fig. 3D). This result suggests that in these cells, cleavage at S2' by TMPRSS2 occurs
249   primarily after uptake into endosomes.
250

251   **Viral membrane fusion requires acidic pH**
252   Endosomes undergo rapid acidification, and acidic pH is a trigger that induces fusogenic
253   conformational changes in many viral envelope proteins. We therefore examined the effect of pH
254   on productive viral entry by adjusting the pH of the medium at 10 minutes post inoculation. From
255   187 traces from VERO-TMPRSS2 cells incubated at pH 6.8, we observed 84 fusion events at the
256   cell surface, as defined by loss of Atto 565 signal and by accompanying eGFP-P delivery into the
257   cytosol (Fig. 3 E-H, S17). The abrupt partial loss of punctate signal, interpreted as S1-fragment
258   release, always preceded fusion (signaled by diffusion in the plasma membrane of the remaining
259   Atto 565 signal with a half-life of about 20 sec) and by eGFP-P delivery into the cytosol, typically
260   within 10 sec (Fig. 3 E, F). We defined eGFP-P delivery into the cytosol by a change in its motion
261   from confined (α <0.8) when on the cell surface to Brownian (0.8< α <1.2) when in the cytosol
262   (Fig. 3G). In the absence of S1-release, we did not detect S1 diffusion or eGFP-P delivery into
263   the cytosol. We conclude that release of S1 and subsequent or concomitant exposure to acidic
264   pH result in release of virion contents into the cell.

9

265

266   Incubation of Vero-TMPRSS2 cells at pH 6.2 rather than 6.8 during inoculation prevented release

267   of the S1-fragment and hence prevented viral fusion at the cell surface (Fig. 3 E, G, and H). This

268   pH dependence is consistent with an expected loss of TMPRSS2 proteolytic activity as the pH

269   falls below 7. When cells were incubated at pH 7.4 throughout infection, we did not observe any

270   particle fusion and content release at the cell surface, even though TMPRSS2 cleavage, as

271   detected by S1-fragment release, still occurred (Fig. 3 E, G and H).

272

273   The efficiency of entry by VSV-SARS-CoV-2 tracked by visualizing content release or by extent

274   of infection increased in Vero-TMPRSS2 cells at pH 6.8 (Fig. 3H). To investigate further the

275   requirement of acidic pH for efficient SARS-CoV-2 S-mediated membrane fusion, we carried out

276   bypass experiments to initiate infection directly at the cell surface. We blocked endocytic uptake

277   into cells with dynasore-OH and exposed bound particles to different pH ranging from 6.2-7.4.

278   Infection of Vero, Caco-2 or Calu-3 cells was blocked regardless of the pH, whereas Vero cells

279   overexpressing TMPRSS2 were readily infected by acid triggering of the S protein at the cell

280   surface (Fig. 3J, S18).

281

282   These results were consistent with the observed lack of release of the S1-fragment from viruses

283   at the surface of Vero, Caco-2, or Calu-3 cells (Fig. 3D). To eliminate a requirement for TMPRSS2

284   cleavage of S, we pre-activated particles by incubation with trypsin before inoculating the cells.

285   These pre-activated particles were as infectious in Vero-E6 TM cells treated with dynasore-OH

286   and inoculated at pH < 7 as non-trypsinized particles in the same cells and conditions. Thus,

287   trypsin and TMPRSS2 cleavages were equally effective in activating the particles. With

288   progressive acidification of the medium, infection increased, reaching a maximum at pH 6.6 and

289   remaining constant to pH 6.2 (Fig. 3H). These results show that S-mediated fusion requires pH <

290   7. We obtained similar results concerning the effect of pH on infectivity of authentic SARS-CoV-

291   2 with cells in which endocytosis was blocked and genome penetration depended solely on cell-

292   surface fusion events (Fig 3I-J).

293

294   **Influence of S protein variation on infectious entry pathways**

295   We found that response to infection inhibitors and the requirement for endocytosis and proteolytic

296   cleavage of S for the VSV chimera with the Delta variant S protein were essentially the same for

297   the chimera with the S protein from the original Wuhan-Hu1 isolate (Fig. 4A-D and S20, S21).

298   Conserved events included release of the S1-fragment from receptor-bound virions attached to

10

299   Vero-TMPRSS2 cells (Fig. 4 B), and S1 release followed by fusion and genome penetration when

300   inoculation was at pH 6.5-6.8 (Fig. 4C). Both Wuhan-Hu1 and Delta also showed enhanced

301   infectivity of Vero-TMPRSS2 cells inoculated at pH 6.8 (Fig. E-G).

302

303   Examination of the entry pathway mediated by the S protein of Omicron varied with the cell type

304   used to produce the virus. VSV-Omicron produced in Vero-TMPRSS2 cells depended on

305   TMPRSS2 activation for infection of Vero-TMPRSS2, although somewhat fewer virions released

306   the S1 fragment at the cell surface (Fig 4B-D). VSV-SARS-CoV-2 chimeras with Omicron S

307   produced in MA104 cells could not be activated by TMPRSS2 and failed to infect or fuse from the

308   surface of Vero-TMPRSS2 cells at pH 6.8 (Fig. 4A-D, S20, S21). Infection required activation by

309   cathepsins for fusion and infection from endosomes (Fig 4 A-D, S20, S21). Trypsin treatment of

310   VSV-SARS-CoV-2-Omicron, which cleaves at both the furin and TMPRSS protease sites (*23*),

311   allowed infection to proceed from the cell surface at acidic pH, independent of the producer cell

312   line, even in the presence of an endocytosis inhibitor (Fig.4A-D, S20, S21).

313

314   Sequence analysis of the genomic RNA from the VSV-SARS-CoV-2 chimeric viruses confirmed

315   the presence of the TMPRSS2 and furin cleavage sites in Omicron S. As furin cleavage in

316   producing cells is essential for subsequent proteolysis by TMPRSS2 in the infecting cell, we

317   tested whether incomplete furin cleavage explained the differential susceptibility to TMPRSS2

318   activation. We found much less cleavage of Omicron S for virus produced in MA104 cells (Fig 4D)

319   than for virus produced in Vero-TMPRSS2 cells (Fig. 4D). Particles with furin cleaved S were

320   susceptible to TMPRSS2 activation (Fig 4A-D), released the S1-fragment (Fig 4A), and fused at

321   pH 6.8 (Fig. 4 B,D).

322

323   **Intranasal pH**

324   Our results suggest that an acidic environment is required for successful infection, found in

325   endosomal compartments and at the surface of TMPRSS2 expressing cells purposely exposed

326   to mildly acidic extracellular pH conditions. Since expression of TMPRSS2 appears to be highly

327   expressed in a subset of cells located in the nasopharyngeal cavity (*24*, *25*), we asked whether

328   this milieu would be acidic. Using a pH catheter placed in the left and right nasal cavities of 17

329   healthy male and female volunteers, we found a mildly acidic pH of around 6.6 (Fig. 4 E), in

330   agreement with earlier measurements (*26*, *27*).

DISCUSSION

We examined how SARS-CoV-2 Wuhan and its variants Delta and Omicron enter host cells using a combination of high-resolution live cell 3D imaging and quantitative assays for viral infectivity. Real-time tracking of single VSV-SARS-CoV-2 chimeric particles by lattice light sheet microscopy allowed us to visualize directly, with a sensitivity and time resolution substantially greater than any previous work, the key early steps of viral infection: virion binding, release of the S1-fragment upon cleavage by TMPRSS2, viral membrane fusion, and genome penetration into the cytosol. These observations revealed a previously unsuspected requirement to fuse by exposure to pH between 6.5 to 6.8, even after priming by TMPRSS2 and the attendant release of S1 and the S2' fragment (Figure 5).

Current understanding, derived in part from earlier work on SARS-CoV, has assumed that the only requirement for low pH was for cathepsin L activity when TMPRSS2 was absent or furin cleavage, a prerequisite for TMPRSS2 digestion, had failed during exit from the producing cell (*1*, *11*, *12*, *28–30*). Our results instead distinguish three complementary routes of productive entry, all of which involve exposure of the entering particle to pH < 6.8. The two principal routes are by uptake and traffic to early endosomes, for TMPRSS2-primed virions, or to late endosomal compartments, for cathepsin cleavage in cells regardless of the presence or absence of TMPRSS2. A third, minor route does not require virion uptake, but instead proceeds entirely at the cell surface, but only if cell attachment is at a pH range between 6.5 and 6.8. These observations define the alternative, multi-step pathways of SARS-CoV-2 entry and restrict the conditions for cell-surface penetration.

The released Atto 565-labeled fragment diffused laterally in the membrane, away from the labeled virion, consistent with our identification of the fragment as S1, which we expect to remain attached to ACE2. The release, which always preceded membrane fusion, was independent of exposure to acidic pH. Its dissociation was necessary but not sufficient for S2 to undergo its full, fusion-promoting conformational change. Release required S2' site cleavage, as evidenced by its absence in the presence of the TMPRSS2 inhibitor, Camostat, and by its absence, even in TMPRSS2 expressing cells, at pH lower than about 6.5, where TMPRSS2 is inactive. Trypsin cleavage in our experiments circumvented TMPRSS2 activity, and we indeed observed fusion at pH as low as 6.2.

12

364 The structure of the spike protein and the distribution of lysine residues suggest that most of the
365 Atto 565 label will be on S1 and hence, from the fraction of total label released, that about 25%
366 of the S-protein trimers will have shed S1 upon interaction with membrane bound ACE2,
367 assuming that dissociation of the 3 S1 fragments is cooperative. We estimate from the ratios of
368 stained band intensities on SDS-PAGE that the VSV chimeras have 15-20 S trimers on their
369 surface, and we infer from these numbers that on average, 3-4 spike will have lost S1, liberating
370 their S2 fragments to extend and interact with the host-cell membrane. This estimate is consistent
371 with the likely fraction of the virion surface that makes contact with the cell membrane and with
372 the dependence of S1 shedding from a trimer on its binding to ACE2. It is also consistent with the
373 number of active fusion proteins on other viruses, including VSV itself, required for fusion to
374 proceed (*31–34*).

375

376 Syncytium formation between cells expressing SARS-CoV-2 spike and cells expressing ACE2,
377 often used as a spike-mediated fusion assay, does not appear to depend upon acidic pH. But
378 the interface between the two cells will have vastly more spike protein than the interface between
379 a virus and a target cell. Thus, even low probability S1 dissociation events should be sufficient to
380 create a fusion pore, which can widen and spread across the entire cell-cell junction.

381

382 Release of S1 from a spike also detaches that spike from ACE2. Because cleavage at the S2'
383 site was complete in our experiments, any spike bound by ACE2 would probably have released
384 S1.   Continued association with the host cell would thus have depended on formation of
385 alternative contacts as S1 dissociates. We propose that formation of an extended intermediate
386 and insertion of the S2 fusion peptides into the host-cell membrane creates the interactions that
387 retain the virion at the cell surface. This proposal further implies that protonation of one or more
388 S2 residues at acidic pH then enables S2 to collapse toward the folded-back, post fusion trimer
389 of hairpins and pull together the viral and host-cell lipid bilayers.

390

391 The Omicron variant is more refractory to furin cleavage than previously isolated strains. Its entry
392 pathway will thus depend on the level of furin activity in the producing cells. We indeed found
393 that when grown in Vero-TMPRSS2 cells, Omicron VSV chimeras were susceptible to S2'
394 cleavage by TMPRSS2 and entered from early endosomes or at the cell surface at mildly acidic
395 pH, but when grown in MA104 cells, they required cathepsin cleavage in late endosomes for
396 entry. With authentic SARS-CoV-2 virus, TMPRSS2 susceptibility similarly depended on the cells

13

397   in which the virus was propagated. These observations resolve some ambiguities in the literature

398   concerning the role of TMPRSS2 in Omicron infection (*35–37*).

399

400   Together with differential protease activities, the pH of respiratory mucosa could also influence

401   viral tropism. The pH of the airway-facing surface of the nasal cavity is between 6.2 and 6.8 (our

402   observations and (*26*). Thus, in principle, rapid entry could occur at the surface of TMPRSS2-

403   expressing cells in the nose. In other parts of the nasopharyngeal cavity and in the lung, the pH

404   is neutral (*38*), and we would not expect virus to fuse in those tissues until its endocytic uptake.

405

406   Our suggestion that at neutral pH, a relatively long-lived, extended S2 intermediate may be

407   present at the virus-cell interface bears both on potential therapeutic interventions and on the

408   availability of otherwise occluded epitopes to mucosal antibodies. Persistence of an extended

409   intermediate after gp120 release during HIV entry is thought to account for inhibition of viral

410   infectivity by the peptide fusion inhibitor entfuvirtide and for neutralization by antibodies that

411   recognize epitopes unavailable on a prefusion Env trimer. Our results are consistent with

412   observations that comparable interventions can impede SARS-CoV-2 infection in animal models

413   (*39*).

414 **MATERIAL AND METHODS**

415 **Materials and Cells**

416 All materials and cells used in this study are described in detail in Supplementary Appendix S1.

417

418 **Generation of VSV-SARS-CoV-2 chimeras**

419 The generation of a replication competent recombinant VSV chimera expressing eGFP where the

420 glycoprotein G was replaced with spike (S) protein Wuhan-Hu-1 strain (VSV-eGFP-SARS-CoV-

421 2) has been described (*13*). Additional details for the generation of the VSV recombinants

422 expressing eGFP and SARS-CoV-2 spike variants for Delta (B.1.617.2) and Omicron (B.1.1.529)

423 are described in Supplementary Appendix S1.

424

425 **Generation of SVG-A cells expressing ACE2 and TMPRSS2**

426 SVG-A cells ectopically expressing ACE2 and TMPRSS2 were generated by lentivirus

427 transduction. Briefly, lentivirus encoding human ACE2 or TMPRSS2 were generated as follows:

428 HEK293T packaging cells were seeded at 3.8×10^6 cells in a 10 cm tissue culture plate and grown

429 in complete DMEM supplemented with 10% v/v FBS at 37 °C and 5% CO_2.

430

431 Transfection mixtures containing 90 µL lipofectamine 3000 (Thermo Scientific L3000001),

432 psPAX2 (1.3 pmol; Addgene #12260), pMD2.G (0.72 pmol; Addgene #12259) and

433 TMPRSS2/pLX304 or ACE2/pLJM1 (1.64 pmol; gifts from Sean Whelan) 90 µL lipofectamine

434 3000 (Thermo Scientific L3000001), 1ul psPAX2 (1.3 pmol; Addgene #12260), 0.6 ul pMD2.G

435 (0.72 pmol; Addgene #12259) and 1.2 ul TMPRSS2/pLX304 or ACE2/pLJM1 (1.64 pmol) in 5 ml

436 OptiMEM medium (Thermo Scientific 31985062) mixed by pipetting and incubated for 20 minutes

437 at room temperature. 0.7 million cells were plated in a 10 cm plate 18 hr prior to transfection; the

438 medium was then replaced with the entire transfection mixture and cells incubated for 6 hours at

439 37°C, after which the medium was replaced with 15 ml complete DMEM medium. After 12 hours,

440 this medium was replaced with 15 ml of complete DMEM medium, which was then harvested 24

441 hr later after further growth. After addition of another 15 ml of medium, cells and virus were

442 allowed to growth, ending with a second harvest of medium. The medium was cleared of debris

443 by centrifugation at 5000 x g for 5 mins at room temperature and supernatants containing

444 lentivirus stored at -80°C.

445

446 Ectopic stably expression of ACE2 and TMPRSS2 was achieved by transduction of SVG-A cells

447 (gift from Walter J. Atwood, Brown University) gene-edited to simultaneously express

448   fluorescently tagged early and late endosomal markers EEA1 and NPC1 fused to mScarlett or

449   Halo, respectively (*21*). Briefly, SVG-A 1x10^6 cells were seeded in a well from a 6-well plate and

450   grown overnight in MEM media with 10% FBS. Cleared medium containing ACE2 or TMPRSS2

451   lentivirus (1 mL) was added to the cells and incubated for 16 h, following replacement with fresh

452   medium cells were incubated for additional 24 hrs. Cells were allowed to grow for another 4 days

453   in the presence of 7 µg/mL puromycin to select for ACE2 expressing cells or 5 µg/mL blasticidin

454   for TMPRSS2 expressing cells. Surviving cells were grown in the absence of puromycin of

455   blasticidin for 4 days and cell stocks frozen and kept in liquid nitrogen. SVG-A cells

456   simultaneously stably expressing ACE2 and TMPRSS2 were obtained by transduction with

457   lentivirus encoding TMPRSS2 and selection with Blasticidin of cells stably expressing ACE2.

458

459   **Preparation of VSV chimeras for imaging and infection experiments**

460   All VSV-SARS-CoV-2 variants were grown in MA104 cells in 15 to 20 150-mm dishes and infected

461   at a multiplicity of infection (MOI) of 0.01 as previously described (*9, 13*) in addition to the Omicron

462   variant also grown in Vero TMPRSS2 cells. Briefly, media containing the viruses were collected

463   72 hours post infection and clarified by centrifugation at 1,000 x g for 10 min at 4°C. A pellet with

464   virus and extracellular particles was obtained by centrifugation in a Ti45 fixed-angle rotor at

465   72,000 x g (25,000 rpm) for 2 hours at 4°C, then resuspended overnight in 0.5 mL PBS at 4°C.

466   This solution was layered on top of a 15% sucrose-PBS solution and a pellet with virions obtained

467   by centrifugation in a SW55 swinging-bucket rotor at 148,000 x g (35,000 rpm) for 2 hours at 4°C.

468   The resulting pellet was resuspended overnight in 0.4 mL PBS at 4°C, layered on top of a 15 to

469   45% sucrose-PBS linear gradient and subjected to centrifugation in a SW55 swinging-bucket rotor

470   at 194,000 x g (40,000 rpm) for 1.5 hours at 4°C. The predominant light scattering band located

471   in the lower one-third of the gradient and containing the virions was removed by side puncture of

472   the gradient tube. Approximately 0.3 ml of this solution was mixed with 25 ml of PBS and

473   subjected to centrifugation in a Ti60 fixed-angle rotor at 161,000 x g (40,000 rpm) for 2 hours at

474   4°C. The final pellet was resuspended overnight in 0.2 - 0.5 mL PBS aliquoted and stored frozen

475   at -80°C for use in subsequent imaging and infection experiments, without detectable change in

476   infectivity.

477

478   **Isolation and propagation of SARS-CoV-2**

479   A human isolate of SARS-CoV-2, Wuhan (B.1) was obtained in accordance with the protocol

480   approved by the Helsinki University Hospital laboratory research permit 30 HUS/32/2018§16.

481   Briefly, a nasopharyngeal swabs from a patient infected with COVID19 was suspended in 0.5 ml

482   of universal transport medium (UTM®, Copan Diagnostics) and used to inoculate Vero TMPRSS2*

483   cells for 1 h at 37°C, after which the inoculum was replaced with minimum essential medium

484   (MEM) supplemented with 2% heat inactivated FBS, L-glutamine, penicillin, and streptomycin and

485   virus allowed to grow for 48 hr. Virions in the supernatant (P0) were subjected to a similar second

486   round of propagation (P1), analyzed by DNA sequencing, and aliquots stored at 80°C in a solution

487   containing MEM, 2% heat inactivated FCS, 2 mM L-glutamine, and 1% penicillin-streptomycin.

488   Extent of virus replication was determined by real-time PCR (RT-PCR) using primers for SARS-

489   CoV-2 RNA-dependent RNA polymerase (RdRP) (*40*).

490

491   **VSV-eGFP-SARS-CoV-2 infection assays**

492   Infection assays for the Wuhan, Delta or Omicron VSV-eGFP-SARS-CoV-2 chimeras were done

493   at a final ~ 80% confluency of cells plated one day before the infection assay as previously

494   described (*9*) and further explained in Supplementary Appendix S1.

495

496   **SARS-CoV-2 infection assays**

497   All experiments with SARS-CoV-2 were performed in biosafety level 3 (BSL3) facilities at the

498   University of Helsinki with appropriate institutional permits. Virus samples were obtained under

499   Helsinki University Hospital laboratory research permit 30 HUS/32/2018§16. Infections were

500   carried for 16 hours at 37°C with 5% CO_2. Cells were then fixed with 4% paraformaldehyde in

501   PBS for 30 min at room temperature before being processed for immunodetection of viral N

502   protein, automated fluorescence imaging, and image analysis. The detailed protocol is outlined in

503   the Supplementary Appendix S1.

504

505   **VSV-SARS-CoV-2 Atto 565 labeling and single molecule Atto 565 dye calibration**

506   Stock solutions of VSV-SARS-CoV-2 and its variants at a concentration of ~150 µg/ml viral RNA

507   were conjugated with Atto 565-NHS ester (Sigma-Aldrich, cat. 72464) as previously described

508   (*41*). The number of Atto 565 molecules attached to a single virion was determined by comparing

509   the total fluorescence intensities associated with a given virion and the fluorescence intensity

510   associated with the last bleaching step of the same virion, as previously described (*42, 43*). A

511   brief description of these steps are outlined in the Supplementary Appendix S1.

512

513   **Trypsin cleavage of VSV-eGFP-SARS-CoV-2**

514   VSV-eGFP-SARS-CoV-2 and variants (as indicated in text) at a concentration 30 µg/mL virus

515   RNA in a total volume of 100 µL in DMEM with 25 mM HEPES, pH 7.4 were incubated for 30 min

516 at 37°C with 1 µg/mL trypsin (Pierce trypsin, TPCK treated from Thermo scientific cat. PI20233).

517 Trypsin activity was terminated with 10 µM Aprotinin (bovine lung, Sigma-Aldrich cat. A1153). The

518 required concentration of trypsin was determined by trypsin serial dilution, aiming for the largest

519 infectivity Vero cells whose endogenous cathepsin proteases activity had been inhibited with 20

520 µM E-64 (Figure S19). Infections were done with VSV or its variants at a concentration of 0.5

521 µg/mL (for Vero and Vero TMPRSS2) or 5 µg/mL virus RNA (for Caco-2 or Calu-3). When

522 required, the trypsin cleaved VSV's were used together with infection inhibitors or for pH bypass

523 experiments as described above.

524

525 ***In vitro* release of S1 from trypsin activated VSV-SARS-CoV-2**

526 VSV-eGFP-SARS-CoV-2-Atto 565 was incubated with trypsin at various concentrations for 30

527 min and the reaction stopped by addition of aprotinin to a final concentration of 10 µM. Virus was

528 then used to infect Vero cells with endogenous cathepsin proteases inhibited with 20 µM E-64 to

529 determine maximum concentration of trypsin required to proteolytically activate the virus.   Virus

530 either without or with trypsin cleavage, or with ACE2 bound before and after trypsin cleavage

531 were plated onto a poly-D-lysine coated glass to determine the number of Atto 565 fluorescence

532 dyes associated with each one of the single particles using spinning disc confocal microscopy. At

533 least 8,000 particles were imaged per experimental condition to guarantee the ability to distinguish

534 intensity losses of at least 20%. Every experimental condition was repeated in triplicate and the

535 intensity of the mean intensities of the peak Gaussian fit was used to determine the after and

536 deviation of Atto565 dyes per condition, Figure S19.

537

538 A computation simulation was performed to validate the ability to detect with statistical

539 significance a 20% fluorescence intensity loss approximate equivalent to the 20-30% loss

540 observed *in vivo* with virions when attached to the cell surface of Vero TMPRSS2. Experimental

541 data corresponding to 8,845 undigested control virions were used to generate a probability density

542 function from which 9 fit parameters (3 mean intensities with corresponding sigmas and the

543 relative contribution to the distribution) were obtained by fitting the sum of 3 Gaussian

544 distributions. These parameters were then used to generate 8845 random numbers of the same

545 distribution and compared to the experimental data set to illustrate the accuracy of the simulation.

546 A second set of 8845 random numbers were generated with mean intensities reduced by 20%, to

547 generate a probability density distribution representing the fluorescence intensities after ACE2

548 mediated release of S cleavage by TMPRSS2.

549

550 **Nasal pH and temperature measurements**

551 The pH and temperature of the nasal cavity, close to the under lower turbinate, from each nostril

552 from 17 healthy volunteers, age 26-55, males and females, were determined using a Digitrapper

553 pH 400 recorder (Medtronic) connected to a single-use Versaflex disposal dual sensor pH

554 catheter (Medtronic) and a Beurer FT 15/1digital thermometer (Beurer), respectively. The

555 temperature dependent pH response of the Digtrapper was corrected to consider the temperature

556 in the nostrils determined for each volunteer.

557

558 These measurements were obtained under the ethical permit n. HUS/2502/2020 granted by the

559 ethical committee of Helsinki and Uusimaa hospital district to Ahmed Geneid and Markku Patjas

560 at the Helsinki University Hospital.

561

562 **Preparation of glass coverslips**

563 Infection and uptake assays of VSV-eGFP-SARS-CoV-2 and VSV-P-eGFP-SARS-CoV-2 done

564 by spinning disc confocal microscopy visualization, were performed using 25 mm #1.5 coverslips

565 bound with polydimethylsiloxane (PDMS) of about 1 mm in thickness and of 3 mm (infection) or

566 5 mm (uptake) in diameter wells punched as previously described (*9*) (see also in Supplementary

567 Appendix S1).

568

569 **Live cell spinning disc-confocal microscopy**

570 Visualization experiments were done with an inverted spinning disc confocal microscope (*42*)

571 following the details described in Supplementary Appendix S1.

572

573 **Live cell lattice light sheet microscopy**

574 Cells were plated in a 35 mm culture dish containing 5 mm in diameter glass coverslips to achieve

575 60% final confluency the day of each experiment. Immediately before lattice light sheet

576 visualization, the cover slip was placed on top of parafilm placed in a 10 cm in diameter petri dish

577 including wet chem wipes to maintain humidity. Approximately 10 µL of a solution containing VSV-

578 SARS-CoV-2 in DMEM with 25 mM HEPES at pH 7.4 for the times indicated in the text, after

579 which the coverslips were transferred to the imaging stage of the LLSM. Visualization was done

580 using phenol red free media, (FluoroBrite™) supplemented with 5% FBS and 25 mM HEPES at

581 the indicated pH. Imaging was done at 37^oC in the presence of 5% CO_2 and 100 nM fluorescent

582 Alexa 647 or Alexa 549 dyes added to the medium to determine the cell boundary. The LLSM

583 was operated in sample scan mode with 0.5 µm spacing between each plane along the z-imaging

19

584   axis and samples imaged as a time series of stacks acquired 1 to 5 sec using dithered multi-
585   Bessel lattice light sheet illumination (*40*, *43*). When using gene edited SVG-A cells expressing
586   EEA1-Scarlett and NPC1-Halo, Halo was first labeled by incubation of the cells with 200 nM
587   JFX646 for 30 minutes at 37°C and 5% CO_2 followed by three 2-minute washes with DMEM
588   containing 10% FBS, 25 mM HEPES, pH 7.4 within 2 hours prior to virus addition to the cover
589   slip. Time series containing 120-300 z-stacks, sequentially obtained every 1-5 sec were acquired
590   with ~ 10 ms exposures per channel.

591

592   The following protocol was used to determine the dwell time between binding of trypsin activated
593   VSV-SARS-CoV-2-Atto 565 Wuhan and release of the S-fragment. Briefly, trypsin activated
594   virions at 5 µg/mL viral RNA were flowed on top of Vero cells plated in a homemade microfluidic
595   flow cell one day prior to the experiment to achieve a 90% confluency. Soluble 100 nM Alexa 549
596   added to the medium was used to determine the cell outline. Samples were imaged with an AO-
597   LLSM microscope configured for sample scan imaging to acquire every 4 sec a stack with planes
598   separated by 0.6 um (0.3 um along the z-optical axis) using an exposure of 3 ms/plane.

599

Single virus tracking and image analysis
601   The 3D stacks obtained using LLSM were deskewed and the diffraction limited spots were
602   detected and tracked in three dimensions using the automated detection algorithms that uses
603   least-squares minimization numerical fitting with a model of the microscope PSF approximated
604   by a 3D Gaussian function and implemented using the MATLAB developed previously (*40*)
605   available   for   download   (https://github.com/VolkerKirchheim/TrackBrowser_Matlab.git).
606   Estimated fluorescent intensities associated with each spot were calculated from the
607   corresponding amplitudes of the fitted 3D Gaussian and compared to those from single virions
608   bound to poly-D-lysine coated glass imaged under the same acquisition conditions and whose
609   dye content was determined by single bleaching steps (*43*).

610

611   Tracks with intensities corresponding to single virus were exported into a custom-made program
612   written   in   LabView   for   visualizing   trajectories   available   for   download
613   (https://github.com/VolkerKirchheim/TrackBrowser_LabView.git).   Each virus trajectory was
614   visually examined for co-localization within a specific compartment (cell surface, EEA1 early
615   endosomes or NPC-1 late endosomes/lysosomes, cytosol) and the mean squared displacements
616   (MSDs) were calculated from all 3D coordinates for all possible time frames within that

20

617   compartment. A non-linear relationship between MSD and time for anomalous diffusion was fitted

618   to the MSD data according to the power law in equation:

619    $$MSD(t) = 6\,K\,t^{\alpha}$$

620   where K is the generalized diffusion coefficient and α is the anomalous exponent.

621

622   **Statistical analysis**

623   An unpaired t-test was used to determine the statistical significance in the difference between

624   control and experimental values.

FIGURE LEGENDS:

Figure 1. **SARS-CoV-2 infection requires endocytosis**

(A) Schematic of live-cell volumetric lattice-light-sheet fluorescence microscopy (LLSM) imaging experiments **(B-G)** used to obtain 3D time series of VSV-eGFP-P-SARS-CoV-2-S-Atto 565 entry into VERO TMPRSS2 cells during early stages of infection using an MOI of 2. For each experiment, three cells were consecutively imaged volumetrically every 4.7 seconds for 10 min.

(B) Maximum intensity projections showing fluorescently tagged VSV-SARS-CoV-2 within 1 um in thickness optical sections from the first frame of the time series acquired for representative cells 1, 2 and 3.

(C) Representative single virion trajectories of VSV-eGFP-P-SARS-CoV-2-S-Atto 565 within a 1 um optical slice of a time series acquired during the first 10-minutes of cell 1. Traces highlight particles at the cell surface (black) and within the cell volume after endocytosis (blue), in both cases containing colocalized eGFP-P and S-Atto 565; it also shows traces in the cytosol (green) containing eGFP-P upon its separation from the Atto565 signal (light blue). Single images highlighting these events are shown in the panels below.

(D) Orthogonal projection of the traced event highlighted in **(C)**.

(E) Representative summary of 266 virion traces analyzed during cell entry. Data from single coverslips (out of five) obtained per each cell type are shown. Vertical traces highlight the transfer of virions from the cell surface to the cell interior (assumed to be in endosomes because the colocalization of the eGFP-P with S-Atto 565 signals) or from endosomes to the cytosol (upon loss of localization of the eGFP-P and S-Atto 565 signals). Events corresponding to step wise loss of the S-Atto 565 signal at the cell surface are indicated (yellow).

(F) Representative plot illustrating the mean squared displacements (MSD) for the trajectory depicted in **(D)** when the particle is at the cell surface (black), in endosomes (blue), or in the cytosol upon separation of eGFP-P (which remains in endosomes, light blue) and S-Atto565 in the cytosol (green).

(G) Summary dot plot showing the diffusion mode (α) for 1692 virion trajectories and corresponding 139 penetration events; all penetration events occurred from endosomes except for one event at the cell surface in a single Vero TMRSS2 cell. The plot highlights the confined motion ($\alpha < 0.80$) of virions at the cell surface, trajected motion ($\alpha > 1.2$) in endosomes, and Brownian motion ($0.80 < \alpha < 1.2$) in the cytosol.

(H-J) Effect of inhibition of endocytosis in the infection by VSV-eGFP-SARS-CoV-2 **(H,I)** or a human isolate of SARS-CoV-2 **(J)**. Top panel shows examples of infection observed in representative fields of Vero TMPRSS2 over expressing or not the dominant negative dynamin

22

659   K44A mutant or treated or not with 40 µM dynasore-OH. Images in the top panels were obtained

660   using spinning disc confocal microscopy and show maximum intensity projections. Results from

661   similar infections obtained with different cell types are shown in the bottom panel. The difference

662   of results between control conditions and inhibition of endocytosis by K44A dynamin

663   overexpression or incubation with dynasore-OH incubation was statistically significant with p

664   value of <0.001 using an unpaired t-test.

665

666   **Figure 2. Endocytic entry routes of VSV-SARS-CoV-2**. VSV-eGFP-P-SARS-CoV-2 was used

667   to infect SVG-A gene-edited to express early endosomal antigen 1 fused to the fluorescent protein

668   Scarlet (EEA1-Scarlett) as an early endosomal marker and for late endosomal/lysosomal

669   compartments a Halo-tagged version of the cholesterol transporter Niemann Pick C1 (NPC1-

670   Halo) together with ectopic expression of ACE2 and TMPRSS2 and volumetrically imaged using

671   LLSM according to Fig. 1.

672   **(A)** Representative 2 µm projection from the first frame of the time series acquired 8-min after

673   inoculation.

674   **(B-E)** Representative examples of single trajectories of VSV-eGFP-P-SARS-CoV-2 highlighting

675   the extent of colocalization between eGFP-P and EEA1 or between eGFP-P and NPC-1 Halo

676   labeled with JFX646 (top panel), the orthogonal projection of the trajectory (middle panel) and

677   corresponding plots for number of VSV particles on the spot, extent of colocalizations and MSD

678   (bottom panels). Additional examples found in related Fig S11-16.

679   **(F)** Representative summary of results for 257 and 373 virion traces analyzed during cell entry

680   from single coverslips (out of a total of five) plated with SVG-A ACE2 or SVG-A ACE2 TMPRSS2.

681   Vertical and diagonal traces highlight the transfer of virions from the cell surface to its interior and

682   associated with early or late endosomes/lysosomes as defined by colocalization of eGFP-P with

683   EEA1-Scarlett or eGFP-P with NPC1-Halo, respectively.

684

685   **Figure 3. Surface entry route of SARS-CoV-2**

686   **(A-G)** VSV-eGFP-P-SARS-CoV-2-S-Atto 565 was used to infect Vero TMPRSS2 cells and used

687   to study the effect by acidic pH in the medium on the TMPRSS2 mediated surface release of the

688   S-fragment, on cellular location of fusion and genome delivery and on infectivity.

689   **(A, B)** Single virion trajectories of VSV-eGFP-P-SARS-CoV-2-Atto565 in a Vero TMPRSS2 cell

690   incubated at pH 6.8 showing in **(A)** an example of S-release at the surface without subsequent

691   fusion and **(B)** an example of S-release followed by penetration of eGFP-P to the cytosol.

692   Orthogonal views of the tracings and corresponding time-dependent fluorescent intensities for S-

693   Atto 565 and eGFP-P are shown.

694   **(C)** Representative summary from 237 virion traces analyzed during cell entry. Data from single

695   coverslips (out of five) obtained per each pH condition in the medium are shown. Vertical traces

696   of cells incubated at 6.8 highlight the efficient transfer of virions from the cell surface to the cell

697   interior (based on loss of signal colocalization between eGFP-P and S-Atto 565 and

698   corresponding change of diffusion from constrained to directed). Events of stepwise partial loss

699   of S-Atto 565 are indicated (yellow). Similar data with cells incubated at pH 6.2 shows

700   accumulation of virions in endosomes, complete absence of fusion events from the cell surface

701   and limited number of fusion events from endosomes.

702   **(D)** Data showing fraction of virions that released the S-fragment from virions at the cell surface

703   of Vero TMPRSS2 cells incubated at pH 6.8 in the absence or presence of 10 uM Camostat, or

704   of Vero E6, Caco-2 or Calu-3 cells also at pH 6.8 and in the absence of Camostat. The difference

705   of results between control and all other conditions was statistically significant with p value of

706   <0.0001 using an unpaired t-test.

707   **(E)** Cumulative plot corresponding to the dwell time between the stepwise partial drop of the S-

708   Atto 565 signal of a virion at the cell surface and fusion defined by surface spreading of the

709   remaining Atto 565 signal and transfer into the cytosol of eGFP-P. Data from 86 traces and from

710   five experiments.

711   **(F)** Effect of extracellular pH on the transfer of eGFP-P of virions from the cell surface (red) or

712   from endosomes (black) to the cytosol.   Each dot represents average +/- std from 5 coverslips

713   with 3 cells imaged per coverslip and at least 600 virus tracked per condition. Line across box

714   represents the median of distribution and the top and bottom represent the quartiles.

715   **(G)** Effect of extracellular pH of the cell medium on the mode of diffusion of the eGFP-P signal

716   associated with a virion before and after delivery from the surface (red) or from endosomes (black)

717   to the cytosol.

718   **(H)** pH bypass infection experiments to test the effect of extracellular acidic pH on the extent of

719   infection of Vero or Vero TMPRSS2 cells by VSV-eGFP-SARS-CoV-2 alone or treated for 30 min

720   with 1 µg/mL trypsin; experiments carried in the absence (top panel) or presence (middle and

721   bottom panels) of 40 uM dynasore-OH. Each data point represents an experiment. In each case,

722   the values determined at pH 6.8 and 7.4 are significantly different with a p value of at least <0.0003

723   using an unpaired t-test.

724   **(I)** pH bypass infection experiment using authentic SARS-CoV-2 and Vero TMPRSS2* cells in the

725   absence or presence of 40 uM dynasore-OH. Each data point represents an experiment. No

24

726 statistical difference was observed in the absence of dynasore-OH between pH 6.8 and pH 7.4

727 (p = 0.13); the difference was statistically significant in the presence of dynasore-OH (p < 0.0001)

728 using an unpaired t-test.

729

730 **Figure 4. Entry routes of VSV-SARS-CoV-2 variants are conserved.**

731 **(A-C)** Effect of extracellular pH and type of cells infected with the indicated variants of VSV-eGFP-

732 P-SARS-CoV-2 on **(A)** the extent of S-fragment release from the cell surface and of **(B)** fusion

733 from the cell surface or **(C)** from endosomes.

734 **(D)** Experiments to determine the effect of extracellular pH on the extent of infection by the Delta

735 and Omicron variants of VSV-SARS-CoV-2 in the presence of 40 uM dynasore-OH. The pH

736 bypass experiments in the right panel were done with trypsin-cleaved virions. The bottom two

737 rows compare results obtained with the Omicron variant grown in MA104 or Vero TMPRSS2 cells.

738 Western Blot showing cleavage states of spike protein of VSV-SARS-CoV-2-Omicron grown in

739 different cell types. The bypass pH experiments in the left panels show statistical differences

740 between pH 6.8 and pH 7.4 (p < 0.0001) for Delta and Omicron grown in Vero TMPRRSS2 and

741 of minimal significance for Omicron grown MA 104 using an unpaired t-test. Similar analysis for

742 the experiments in the right panels show statistical differences between pH 6.8 and pH 7.4 for

743 Delta (p < 0.0001) and Omicron grown in Vero TMPRRSS2 (p < 0.0001) and also for Omicron (P

744 = 0.0015) grown in MA 104.

745 **(E)** Nasal pH values determined from 17 healthy individuals. Each dot represents a single pH

746 determination by the pH catheter at the lower turbinate of the right and left nostrils.

747

748 **Figure 5. Schematic representation of the principal entry routes SARS-CoV-2 uses for**

749 **infection.** Entry starts with membrane attachment and ends with spike-protein (S) catalyzed

750 membrane fusion releasing the viral contents into the cytosol. Fusion activity depends on two

751 proteolytic cleavage steps, one typically carried out by furin in the producing cell and the second

752 by TMPRSS2 on the cell surface on in endosomes of the target cell. Alternatively, endosomal

753 cathepsins can carry out both cleavages. Exposure of the virus to an acidic milieu is essential for

754 membrane fusion, genome penetration, and productive infection. Fusion and penetration occur

755 only in acidic early and late endosomal/lysosomal compartments but not at the cell surface, even

756 when the furin and TMPRSS2 cleavages have both occurred. Fusion and penetration can occur

757 at the cell surface of cells expressing TMPRSS2 if the extracellular pH is ~6.8.

758

25

REFERENCES

1. M. Hoffmann, H. Kleine-Weber, S. Schroeder, N. Krüger, T. Herrler, S. Erichsen, T. S. Schiergens, G. Herrler, N.-H. Wu, A. Nitsche, M. A. Müller, C. Drosten, S. Pöhlmann, SARS-CoV-2 Cell Entry Depends on ACE2 and TMPRSS2 and Is Blocked by a Clinically Proven Protease Inhibitor. *Cell*. 181, 271-280.e8 (2020).

2. D. Wrapp, N. Wang, K. S. Corbett, J. A. Goldsmith, C.-L. Hsieh, O. Abiona, B. S. Graham, J. S. McLellan, Cryo-EM structure of the 2019-nCoV spike in the prefusion conformation. *Science*. 367, 1260–1263 (2020).

3. J. Yang, S. J. L. Petitjean, M. Koehler, Q. Zhang, A. C. Dumitru, W. Chen, S. Derclaye, S. P. Vincent, P. Soumillion, D. Alsteens, Molecular interaction and inhibition of SARS-CoV-2 binding to the ACE2 receptor. *Nat Commun*. 11, 4541 (2020).

4. R. Yan, Y. Zhang, Y. Li, L. Xia, Y. Guo, Q. Zhou, Structural basis for the recognition of SARS-CoV-2 by full-length human ACE2. *Sci New York N Y*. 367, 1444–1448 (2020).

5. J. Shang, Y. Wan, C. Luo, G. Ye, Q. Geng, A. Auerbach, F. Li, Cell entry mechanisms of SARS-CoV-2. *P Natl Acad Sci Usa*. 117, 11727–11734 (2020).

6. C. B. Jackson, M. Farzan, B. Chen, H. Choe, Mechanisms of SARS-CoV-2 entry into cells. *Nat Rev Mol Cell Biology*. 23, 3–20 (2022).

7. B. A. Johnson, X. Xie, A. L. Bailey, B. Kalveram, K. G. Lokugamage, A. Muruato, J. Zou, X. Zhang, T. Juelich, J. K. Smith, L. Zhang, N. Bopp, C. Schindewolf, M. Vu, A. Vanderheiden, E. S. Winkler, D. Swetnam, J. A. Plante, P. Aguilar, K. S. Plante, V. Popov, B. Lee, S. C. Weaver, M. S. Suthar, A. L. Routh, P. Ren, Z. Ku, Z. An, K. Debbink, M. S. Diamond, P.-Y. Shi, A. N. Freiberg, V. D. Menachery, Loss of furin cleavage site attenuates SARS-CoV-2 pathogenesis. *Nature*. 591, 293–299 (2021).

8. R. Zang, M. F. G. Castro, B. T. McCune, Q. Zeng, P. W. Rothlauf, N. M. Sonnek, Z. Liu, K. F. Brulois, X. Wang, H. B. Greenberg, M. S. Diamond, M. A. Ciorba, S. P. J. Whelan, S. Ding, TMPRSS2 and TMPRSS4 promote SARS-CoV-2 infection of human small intestinal enterocytes. *Sci Immunol*. 5, eabc3582 (2020).

9. A. J. B. Kreutzberger, A. Sanyal, R. Ojha, J. D. Pyle, O. Vapalahti, G. Balistreri, T. Kirchhausen, Synergistic Block of SARS-CoV-2 Infection by Combined Drug Inhibition of the Host Entry Factors PIKfyve Kinase and TMPRSS2 Protease. *J Virol*. 95, e0097521 (2021).

10. X. Ou, Y. Liu, X. Lei, P. Li, D. Mi, L. Ren, L. Guo, R. Guo, T. Chen, J. Hu, Z. Xiang, Z. Mu, X. Chen, J. Chen, K. Hu, Q. Jin, J. Wang, Z. Qian, Characterization of spike glycoprotein of SARS-CoV-2 on virus entry and its immune cross-reactivity with SARS-CoV. *Nat Commun*. 11, 1620 (2020).

11. T. P. Peacock, D. H. Goldhill, J. Zhou, L. Baillon, R. Frise, O. C. Swann, R. Kugathasan, R. Penn, J. C. Brown, R. Y. Sanchez-David, L. Braga, M. K. Williamson, J. A. Hassard, E. Staller, B. Hanley, M. Osborn, M. Giacca, A. D. Davidson, D. A. Matthews, W. S. Barclay, The furin

797   cleavage site in the SARS-CoV-2 spike protein is required for transmission in ferrets. *Nat*
798   *Microbiol*. 6, 899–909 (2021).

799   12. D. Bestle, M. R. Heindl, H. Limburg, T. V. L. van, O. Pilgram, H. Moulton, D. A. Stein, K.
800   Hardes, M. Eickmann, O. Dolnik, C. Rohde, H.-D. Klenk, W. Garten, T. Steinmetzer, E.
801   Böttcher-Friebertshäuser, TMPRSS2 and furin are both essential for proteolytic activation of
802   SARS-CoV-2 in human airway cells. *Life Sci Alliance*. 3, e202000786 (2020).

803   13. J. B. Case, P. W. Rothlauf, R. E. Chen, Z. Liu, H. Zhao, A. S. Kim, L.-M. Bloyet, Q. Zeng, S.
804   Tahan, L. Droit, Ma. X. G. Ilagan, M. A. Tartell, G. Amarasinghe, J. P. Henderson, S. Miersch,
805   M. Ustav, S. Sidhu, H. W. Virgin, D. Wang, S. Ding, D. Corti, E. S. Theel, D. H. Fremont, M. S.
806   Diamond, S. P. J. Whelan, Neutralizing Antibody and Soluble ACE2 Inhibition of a Replication-
807   Competent VSV-SARS-CoV-2 and a Clinical Isolate of SARS-CoV-2. *Cell Host Microbe*. 28,
808   475-485.e5 (2020).

809   14. B.-C. Chen, W. R. Legant, K. Wang, L. Shao, D. E. Milkie, M. W. Davidson, C.
810   Janetopoulos, X. S. Wu, J. A. H. III, Z. Liu, B. P. English, Y. Mimori-Kiyosue, D. P. Romero, A.
811   T. Ritter, J. Lippincott-Schwartz, L. Fritz-Laylin, R. D. Mullins, D. M. Mitchell, J. N. Bembenek,
812   A.-C. Reymann, R. Böhme, S. W. Grill, J. T. Wang, G. Seydoux, U. S. Tulu, D. P. Kiehart, E.
813   Betzig, Lattice light-sheet microscopy: Imaging molecules to embryos at high spatiotemporal
814   resolution. *Science*. 346, 1257998 (2014).

815   15. C. J. Bradish, J. B. Kirkham, The Morphology of Vesicular Stomatitis Virus (Indiana C)
816   Derived from Chick Embryos or Cultures of BHK21/13 Cells. *Microbiology+*. 44, 359–371
817   (1966).

818   16. D. K. Cureton, R. H. Massol, S. P. J. Whelan, T. Kirchhausen, The Length of Vesicular
819   Stomatitis Virus Particles Dictates a Need for Actin Assembly during Clathrin-Dependent
820   Endocytosis. *Plos Pathog*. 6, e1001127 (2010).

821   17. J. Klumperman, G. Raposo, The Complex Ultrastructure of the Endolysosomal System. *Csh*
822   *Perspect Biol*. 6, a016857 (2014).

823   18. S. M. Ferguson, P. D. Camilli, Dynamin, a membrane-remodelling GTPase. *Nat Rev Mol*
824   *Cell Bio*. 13, 75–88 (2012).

825   19. H. Damke, T. Baba, D. E. Warnock, S. L. Schmid, Induction of mutant dynamin specifically
826   blocks endocytic coated vesicle formation. *J Cell Biology*. 127, 915–934 (1994).

827   20. E. Macia, M. Ehrlich, R. Massol, E. Boucrot, C. Brunner, T. Kirchhausen, Dynasore, a Cell-
828   Permeable Inhibitor of Dynamin. *Dev Cell*. 10, 839–850 (2006).

829   21. Y.-L. Kang, Y. Chou, P. W. Rothlauf, Z. Liu, T. K. Soh, D. Cureton, J. B. Case, R. E. Chen,
830   M. S. Diamond, S. P. J. Whelan, T. Kirchhausen, Inhibition of PIKfyve kinase prevents infection
831   by Zaire ebolavirus and SARS-CoV-2. *Proc National Acad Sci*. 117, 20803–20813 (2020).

832   22. R. Zang, J. B. Case, E. Yutuc, X. Ma, S. Shen, M. F. G. Castro, Z. Liu, Q. Zeng, H. Zhao, J.
833   Son, P. W. Rothlauf, A. J. B. Kreutzberger, G. Hou, H. Zhang, S. Bose, X. Wang, M. D. Vahey,
834   K. Mani, W. J. Griffiths, T. Kirchhausen, D. H. Fremont, H. Guo, A. Diwan, Y. Wang, M. S.

Diamond, S. P. J. Whelan, S. Ding, Cholesterol 25-hydroxylase suppresses SARS-CoV-2 replication by blocking membrane fusion. *P Natl Acad Sci Usa*. 117, 32105–32113 (2020).

23. S. Belouzard, V. C. Chu, G. R. Whittaker, Activation of the SARS coronavirus spike protein via sequential proteolytic cleavage at two distinct sites. *Proc National Acad Sci*. 106, 5871–5876 (2009).

24. Y. Liu, H.-Q. Qu, J. Qu, L. Tian, H. Hakonarson, Expression Pattern of the SARS-CoV-2 Entry Genes ACE2 and TMPRSS2 in the Respiratory Tract. *Viruses*. 12, 1174 (2020).

25. S. P. Sajuthi, P. DeFord, Y. Li, N. D. Jackson, M. T. Montgomery, J. L. Everman, C. L. Rios, E. Pruesse, J. D. Nolin, E. G. Plender, M. E. Wechsler, A. C. Y. Mak, C. Eng, S. Salazar, V. Medina, E. M. Wohlford, S. Huntsman, D. A. Nickerson, S. Germer, M. C. Zody, G. Abecasis, H. M. Kang, K. M. Rice, R. Kumar, S. Oh, J. Rodriguez-Santana, E. G. Burchard, M. A. Seibold, Type 2 and interferon inflammation regulate SARS-CoV-2 entry factor expression in the airway epithelium. *Nat Commun*. 11, 5139 (2020).

26. R. J. A. England, J. J. Homer, L. C. Knight, S. R. Ell, Nasal pH measurement: a reliable and repeatable parameter. *Clin Otolaryngology Allied Sci*. 24, 67–68 (1999).

27. B.-G. Kim, J.-H. Kim, S.-W. Kim, S.-W. Kim, K.-S. Jin, J.-H. Cho, J.-M. Kang, S.-Y. Park, Nasal pH in patients with chronic rhinosinusitis before and after endoscopic sinus surgery. *Am J Otolaryng*. 34, 505–507 (2013).

28. I. Glowacka, S. Bertram, M. A. Müller, P. Allen, E. Soilleux, S. Pfefferle, I. Steffen, T. S. Tsegaye, Y. He, K. Gnirss, D. Niemeyer, H. Schneider, C. Drosten, S. Pöhlmann, Evidence that TMPRSS2 Activates the Severe Acute Respiratory Syndrome Coronavirus Spike Protein for Membrane Fusion and Reduces Viral Control by the Humoral Immune Response. *J Virol*. 85, 4122–4134 (2011).

29. G. Simmons, S. Bertram, I. Glowacka, I. Steffen, C. Chaipan, J. Agudelo, K. Lu, A. J. Rennekamp, H. Hofmann, P. Bates, S. Pöhlmann, Different host cell proteases activate the SARS-coronavirus spike-protein for cell–cell and virus–cell fusion. *Virology*. 413, 265–274 (2011).

30. J. K. Millet, G. R. Whittaker, Host cell entry of Middle East respiratory syndrome coronavirus after two-step, furin-mediated activation of the spike protein. *Proc National Acad Sci*. 111, 15214–15219 (2014).

31. D. L. Floyd, J. R. Ragains, J. J. Skehel, S. C. Harrison, A. M. van Oijen, Single-particle kinetics of influenza virus membrane fusion. *Proc National Acad Sci*. 105, 15382–15387 (2008).

32. T. Ivanovic, J. L. Choi, S. P. Whelan, A. M. van Oijen, S. C. Harrison, Influenza-virus membrane fusion by cooperative fold-back of stochastically induced hemagglutinin intermediates. *Elife*. 2, e00333 (2013).

33. L. H. Chao, D. E. Klein, A. G. Schmidt, J. M. Peña, S. C. Harrison, Sequential conformational rearrangements in flavivirus membrane fusion. *Elife*. 3, e04389 (2014).

28

872   34. I. S. Kim, S. Jenni, M. L. Stanifer, E. Roth, S. P. J. Whelan, A. M. van Oijen, S. C. Harrison,
873   Mechanism of membrane fusion induced by vesicular stomatitis virus G protein. *Proc National*
874   *Acad Sci*. 114, E28–E36 (2017).

875   35. B. Meng, A. Abdullahi, I. A. T. M. Ferreira, N. Goonawardane, A. Saito, I. Kimura, D.
876   Yamasoba, P. P. Gerber, S. Fatihi, S. Rathore, S. K. Zepeda, G. Papa, S. A. Kemp, T. Ikeda, M.
877   Toyoda, T. S. Tan, J. Kuramochi, S. Mitsunaga, T. Ueno, K. Shirakawa, A. Takaori-Kondo, T.
878   Brevini, D. L. Mallery, O. J. Charles, T. C.-N. B. C.-19 Collaboration, S. Baker, G. Dougan, C.
879   Hess, N. Kingston, P. J. Lehner, P. A. Lyons, N. J. Matheson, W. H. Ouwehand, C. Saunders,
880   C. Summers, J. E. D. Thaventhiran, M. Toshner, M. P. Weekes, P. Maxwell, A. Shaw, A. Bucke,
881   J. Calder, L. Canna, J. Domingo, A. Elmer, S. Fuller, J. Harris, S. Hewitt, J. Kennet, S. Jose, J.
882   Kourampa, A. Meadows, C. O'Brien, J. Price, C. Publico, R. Rastall, C. Ribeiro, J. Rowlands, V.
883   Ruffolo, H. Tordesillas, B. Bullman, B. J. Dunmore, S. Gräf, J. Hodgson, C. Huang, K. Hunter,
884   E. Jones, E. Legchenko, C. Matara, J. Martin, F. Mescia, C. O'Donnell, L. Pointon, J. Shih, R.
885   Sutcliffe, T. Tilly, C. Treacy, Z. Tong, J. Wood, M. Wylot, A. Betancourt, G. Bower, C. Cossetti,
886   A. D. Sa, M. Epping, S. Fawke, N. Gleadall, R. Grenfell, A. Hinch, S. Jackson, I. Jarvis, B.
887   Krishna, F. Nice, O. Omarjee, M. Perera, M. Potts, N. Richoz, V. Romashova, L. Stefanucci, M.
888   Strezlecki, L. Turner, E. M. D. D. D. Bie, K. Bunclark, M. Josipovic, M. Mackay, H. Butcher, D.
889   Caputo, M. Chandler, P. Chinnery, D. Clapham-Riley, E. Dewhurst, C. Fernandez, A. Furlong,
890   B. Graves, J. Gray, S. Hein, T. Ivers, E. L. Gresley, R. Linger, M. Kasanicki, R. King, S. Meloy,
891   A. Moulton, F. Muldoon, N. Ovington, S. Papadia, C. J. Penkett, I. Phelan, V. Ranganath, R.
892   Paraschiv, A. Sage, J. Sambrook, I. Scholtes, K. Schon, H. Stark, K. E. Stirrups, P. Townsend,
893   N. Walker, J. Webster, T. G. to P. J. (G2P-J. Consortium, E. P. Butlertanaka, Y. L. Tanaka, J.
894   Ito, K. Uriu, Y. Kosugi, M. Suganami, A. Oide, M. Yokoyama, M. Chiba, C. Motozono, H.
895   Nasser, R. Shimizu, K. Kitazato, H. Hasebe, T. Irie, S. Nakagawa, J. Wu, M. Takahashi, T.
896   Fukuhara, K. Shimizu, K. Tsushima, H. Kubo, Y. Kazuma, R. Nomura, Y. Horisawa, K. Nagata,
897   Y. Kawai, Y. Yanagida, Y. Tashiro, K. Tokunaga, S. Ozono, R. Kawabata, N. Morizako, K.
898   Sadamasu, H. Asakura, M. Nagashima, K. Yoshimura, E.-C. Consortium, P. Cárdenas, E.
899   Muñoz, V. Barragan, S. Márquez, B. Prado-Vivar, M. Becerra-Wong, M. Caravajal, G. Trueba,
900   P. Rojas-Silva, M. Grunauer, B. Gutierrez, J. J. Guadalupe, J. C. Fernández-Cadena, D.
901   Andrade-Molina, M. Baldeon, A. Pinos, J. E. Bowen, A. Joshi, A. C. Walls, L. Jackson, D.
902   Martin, K. G. C. Smith, J. Bradley, J. A. G. Briggs, J. Choi, E. Madissoon, K. B. Meyer, P.
903   Mlcochova, L. Ceron-Gutierrez, R. Doffinger, S. A. Teichmann, A. J. Fisher, M. S. Pizzuto, A. de
904   Marco, D. Corti, M. Hosmillo, J. H. Lee, L. C. James, L. Thukral, D. Veesler, A. Sigal, F.
905   Sampaziotis, I. G. Goodfellow, K. Sato, R. K. Gupta, Altered TMPRSS2 usage by SARS-CoV-2
906   Omicron impacts infectivity and fusogenicity. *Nature*. 603, 706–714 (2022).

907   36. H. Zhao, L. Lu, Z. Peng, L.-L. Chen, X. Meng, C. Zhang, J. D. Ip, W.-M. Chan, A. W.-H.
908   Chu, K.-H. Chan, D.-Y. Jin, H. Chen, K.-Y. Yuen, K. K.-W. To, SARS-CoV-2 Omicron variant
909   shows less efficient replication and fusion activity when compared with Delta variant in
910   TMPRSS2-expressed cells. *Emerg Microbes Infec*. 11, 277–283 (2022).

911   37. D. Bojkova, M. Widera, S. Ciesek, M. N. Wass, M. Michaelis, J. Cinatl, Reduced interferon
912   antagonism but similar drug sensitivity in Omicron variant compared to Delta variant of SARS-
913   CoV-2 isolates. *Cell Res*. 32, 319–321 (2022).

914   38. R. M. Effros, F. P. Chinard, The in vivo pH of the extravascular space of the lung. *J Clin*
915   *Invest*. 48, 1983–1996 (1969).

916   39. R. D. de Vries, K. S. Schmitz, F. T. Bovier, C. Predella, J. Khao, D. Noack, B. L. Haagmans,
917   S. Herfst, K. N. Stearns, J. Drew-Bear, S. Biswas, B. Rockx, G. McGill, N. V. Dorrello, S. H.
918   Gellman, C. A. Alabi, R. L. de Swart, A. Moscona, M. Porotto, Intranasal fusion inhibitory
919   lipopeptide prevents direct-contact SARS-CoV-2 transmission in ferrets. *Sci New York N Y*. 371,
920   1379–1382 (2021).

921   40. F. Aguet, S. Upadhyayula, R. Gaudin, Y. Chou, E. Cocucci, K. He, B.-C. Chen, K.
922   Mosaliganti, M. Pasham, W. Skillern, W. R. Legant, T.-L. Liu, G. Findlay, E. Marino, G. Danuser,
923   S. Megason, E. Betzig, T. Kirchhausen, Membrane dynamics of dividing cells imaged by lattice
924   light-sheet microscopy. *Mol Biol Cell*. 27, 3418–3435 (2016).

925   41. A. H. Abdelhakim, E. N. Salgado, X. Fu, M. Pasham, D. Nicastro, T. Kirchhausen, S. C.
926   Harrison, Structural Correlates of Rotavirus Cell Entry. *Plos Pathog*. 10, e1004355 (2014).

927   42. E. Cocucci, F. Aguet, S. Boulant, T. Kirchhausen, The First Five Seconds in the Life of a
928   Clathrin-Coated Pit. *Cell*. 150, 495–507 (2012).

929   43. Y.-Y. Chou, S. Upadhyayula, J. Houser, K. He, W. Skillern, G. Scanavachi, S. Dang, A.
930   Sanyal, K. G. Ohashi, G. D. Caprio, A. J. B. Kreutzberger, T. J. Vadakkan, T. Kirchhausen,
931   Inherited nuclear pore substructures template post-mitotic pore assembly. *Dev Cell*. 56, 1786-
932   1803.e9 (2021).

933   44. Y. Chen, N. C. Deffenbaugh, C. T. Anderson, W. O. Hancock, Molecular counting by
934   photobleaching in protein complexes with many subunits: best practices and application to the
935   cellulose synthesis complex. *Mol Biol Cell*. 25, 3630–3642 (2014).

936

Author contributions:

Alex J.B. Kreutzberger carried all the experiments except those with human SARS-CoV-2 isolates. Louis-Marie Bloyet and Spencer Stumpf generated, characterized, and sequenced the recombinant virus VSV-eGFP-P-SARS-CoV-2 Whuhan. Zhuoming Liu generated, characterized, and sequenced the recombinant viruses VSV-eGFP-SARS-CoV-2 Delta and Omicron. Anwesha Sanyal generated SVGA-A ACE2 and SVGA-A ACE2 TMPRSS2, maintained the cells lines and assisted with infectivity assays. Catherine A. Doyle helped analyzed data and carried out some VSV-SARS-CoV-2 infection assays. Elliott Somerville helped with virus sample preparation for DNA sequence. Gustavo Scanavachi and Anand Saminathan helped collect LLSM imaging data. Giuseppe Di Caprio set up the single particle data analysis pipeline. Volker Kiessling developed the LabVIEW-based viewer, simulated data and produced the single-particle MSD fitting algorithm. Sean P. J. Whelan oversaw the work to generate and characterize the VSV-chimeras, participated in early discussions, and helped edit portions of the manuscript. Giuseppe Balistreri guided the work on SARS-CoV-2 and performed infection assays, imaging, and image analysis.

971   Ravi Ojha performed SARS-CoV-2 infection assays, imaging, and image analysis. Olli Vapalahti

972   coordinated the BSL3 work, provided SARS-CoV-2 and performed virus sequencing.

973   Tom Kirchhausen and Alex J.B. Kreutzberger were responsible for the overall design of the study;

974   Tom Kirchhausen drafted the manuscript with direct input from Alex J.B. Kreutzberger; all authors

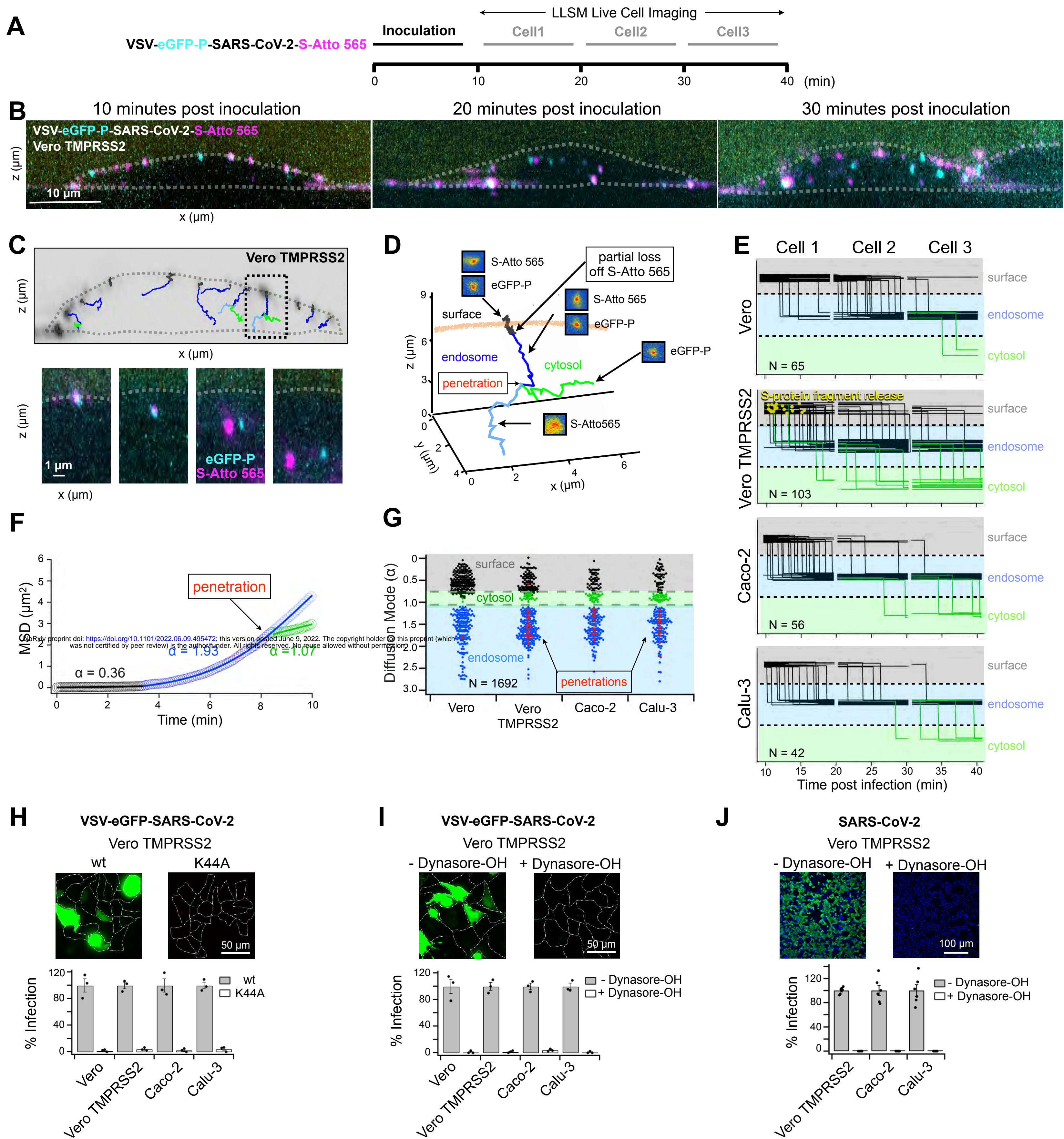975   commented on the manuscript.

976

Competing interests

978   T.K. is a member of the Medical Advisory Board of AI Therapeutics, Inc. The other authors declare
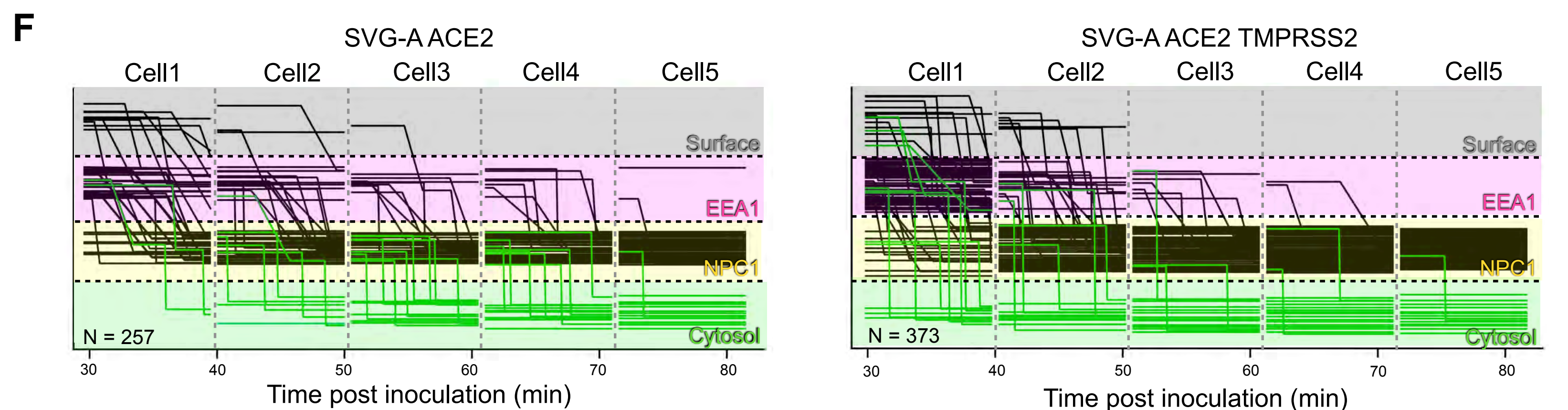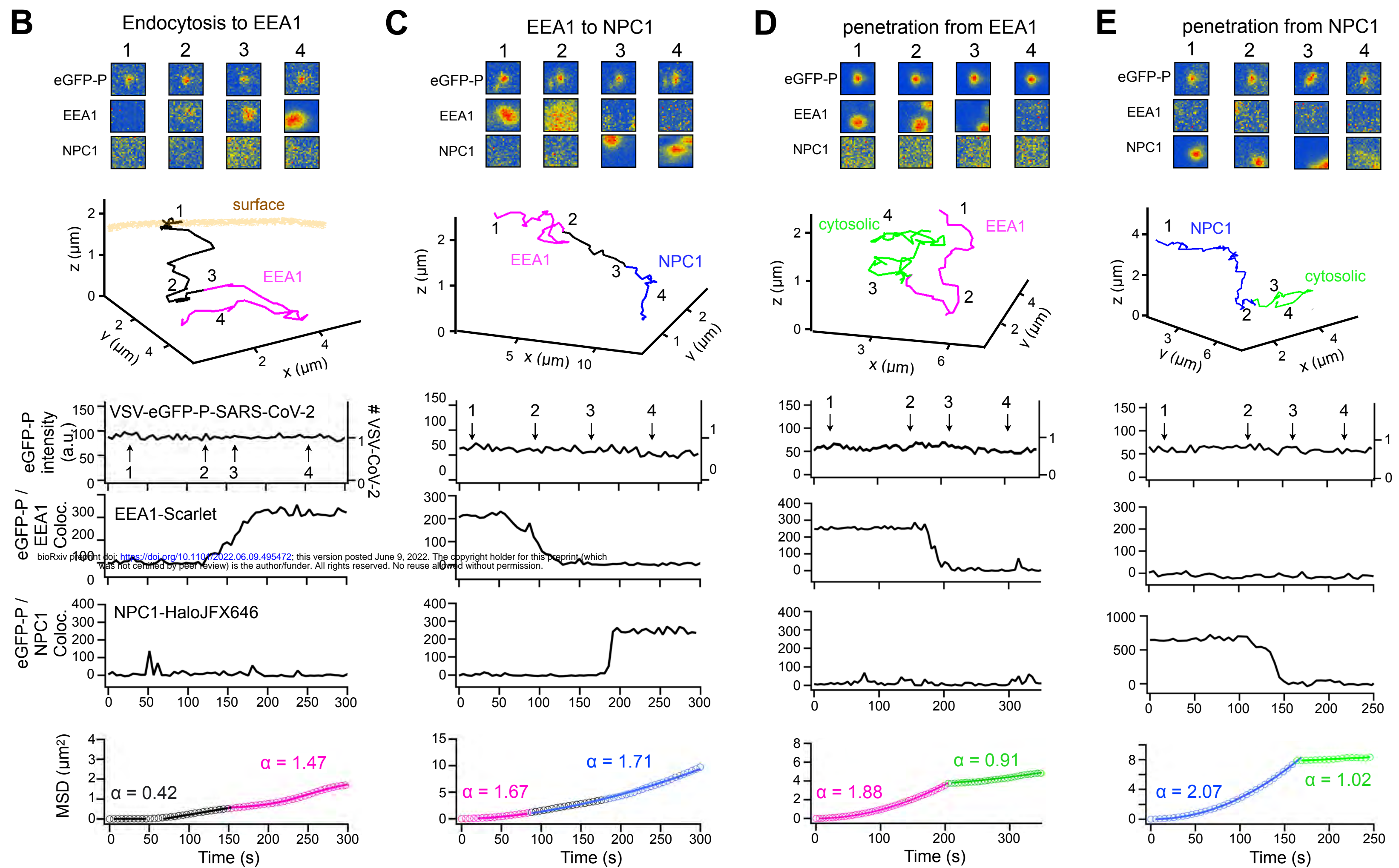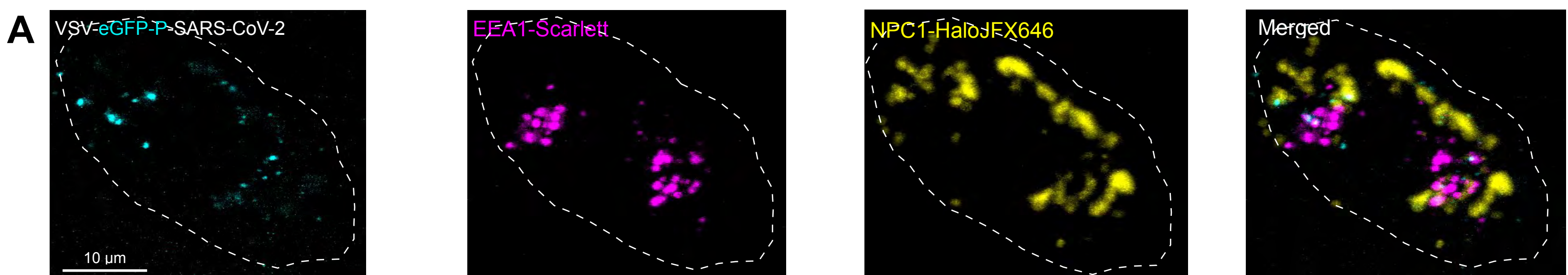
979   no competing interests.

980

Data and material availability

982   All materials and data generated in this study are available upon request. Further information and

983   requests for resources and reagents should be directed to and will be fulfilled by the lead contact,

984   Dr. Tom Kirchhausen, mailto:kirchhausen@crystal.harvard.edu. Requests for VSV-SARS-CoV-2

985   chimeras and their materials transfer agreements (MTA) should be directed to and will be fulfilled

986   by Dr. Sean Whelan, spjwhelan@wustl.edu. This study did not generate any unique large-scale

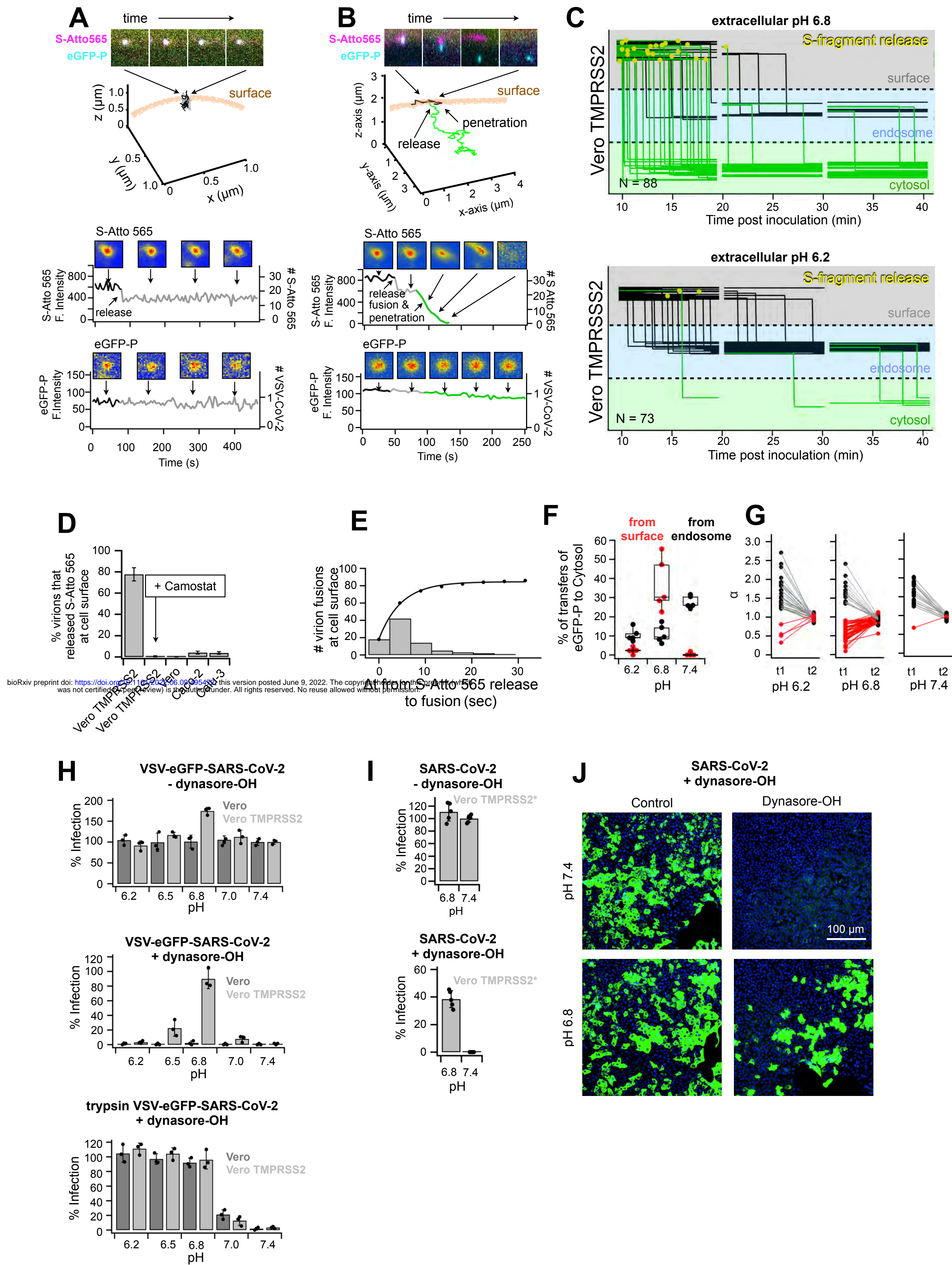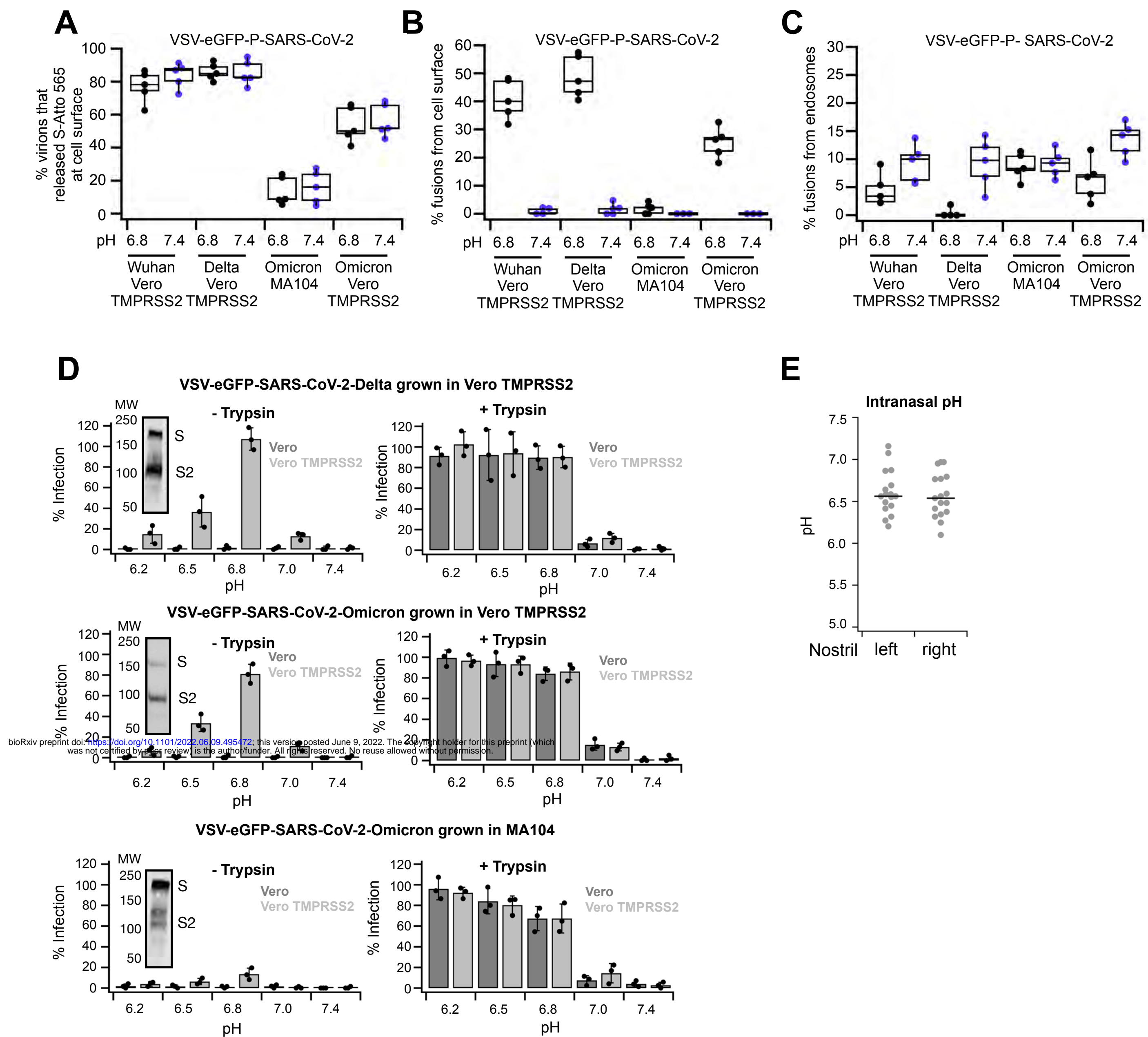987   datasets. The LabView code for visualizing trajectories is available for download (GITHUB).
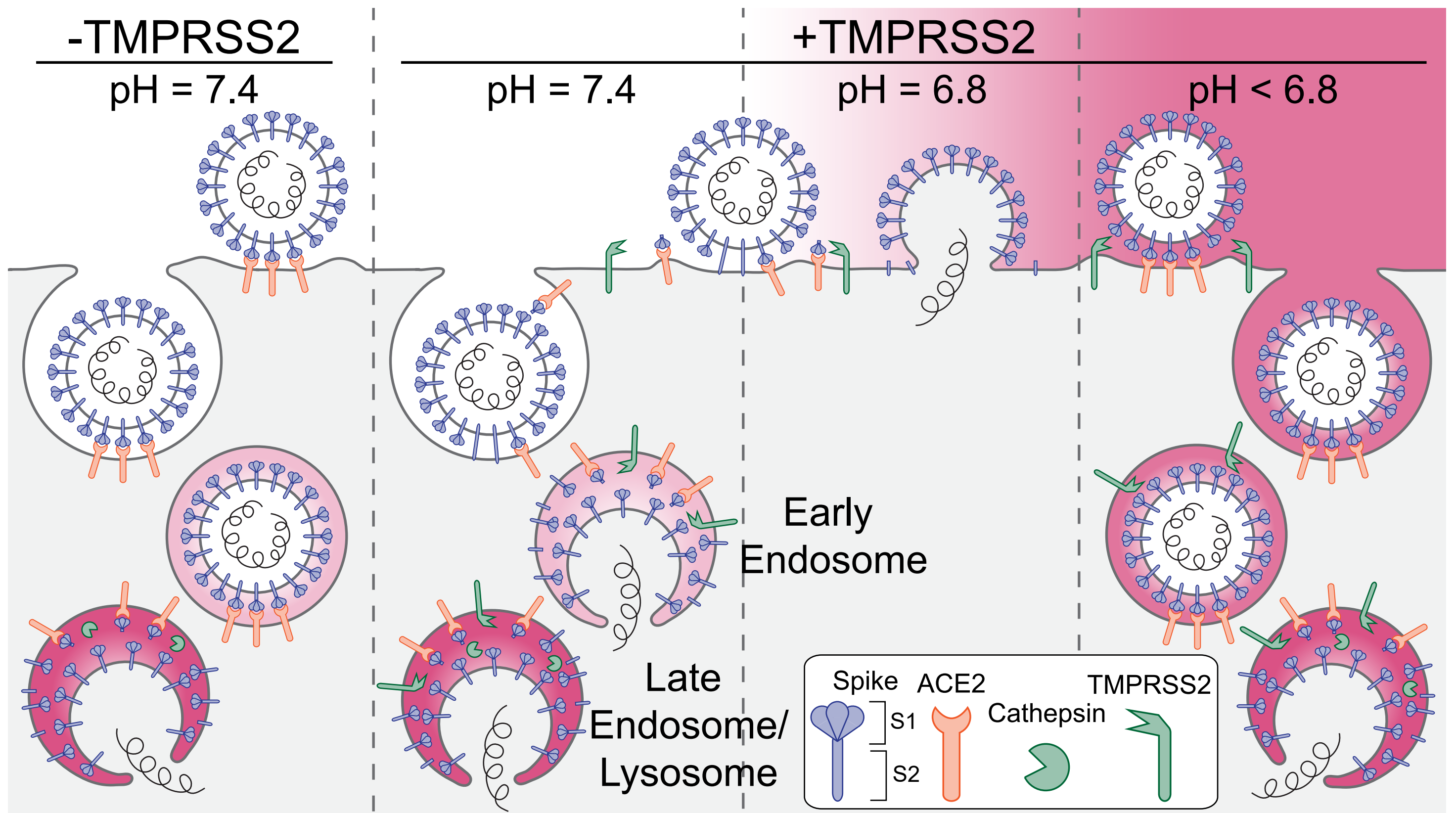
Figure 1

A

VSV-eGFP-P-SARS-CoV-2   EEA1-Scarlett   NPC1-HaloJFX646   Merged

10 µm

B Endocytosis to EEA1   **C** EEA1 to NPC1   **D** penetration from EEA1   **E** penetration from NPC1

F

SVG-A ACE2

Cell1   Cell2   Cell3   Cell4   Cell5

Surface

EEA1

NPC1

N = 257

Cytosol

30   40   50   60   70   80

Time post inoculation (min)

SVG-A ACE2 TMPRSS2

Cell1   Cell2   Cell3   Cell4   Cell5

Surface

EEA1

NPC1

N = 373

Cytosol

30   40   50   60   70   80

Time post inoculation (min)

Figure 2

Figure 3

A VSV-eGFP-P-SARS-CoV-2

B VSV-eGFP-P-SARS-CoV-2

C VSV-eGFP-P- SARS-CoV-2

D

VSV-eGFP-SARS-CoV-2-Delta grown in Vero TMPRSS2

VSV-eGFP-SARS-CoV-2-Omicron grown in Vero TMPRSS2

VSV-eGFP-SARS-CoV-2-Omicron grown in MA104

E Intranasal pH

Figure 4

-TMPRSS2

pH = 7.4

+TMPRSS2

pH = 7.4　　　pH = 6.8　　　pH < 6.8

Early Endosome

Late Endosome/ Lysosome

Spike　ACE2　　　　TMPRSS2

Cathepsin

S1

S2

Figure 5